*J. Fluid Mech.* (2009), *vol.* 637, *pp.* 387–424.  
doi:10.1017/S0022112009990589

# Turbulence structure above a vegetation canopy

JOHN J. FINNIGAN[1]†, ROGER H. SHAW[2] AND EDWARD G. PATTON[3]

[1]CSIRO Marine and Atmospheric Research, GPO Box 3023, Canberra, ACT 2601, Australia
[2]University of California, Davis, CA 95616, USA
[3]National Center for Atmospheric Research, PO Box 3000, Boulder, CO 80307-3000, USA

(Received 22 July 2008; revised 21 May 2009; accepted 21 May 2009)

We compare the turbulence statistics of the canopy/roughness sublayer (RSL) and the inertial sublayer (ISL) above. In the RSL the turbulence is more coherent and more efficient at transporting momentum and scalars and in most ways resembles a turbulent mixing layer rather than a boundary layer. To understand these differences we analyse a large-eddy simulation of the flow above and within a vegetation canopy. The three-dimensional velocity and scalar structure of a characteristic eddy is educed by compositing, using local maxima of static pressure at the canopy top as a trigger. The characteristic eddy consists of an upstream head-down sweep-generating hairpin vortex superimposed on a downstream head-up ejection-generating hairpin. The conjunction of the sweep and ejection produces the pressure maximum between the hairpins, and this is also the location of a coherent scalar microfront. This eddy structure matches that observed in simulations of homogeneous-shear flows and channel flows by several workers and also fits with earlier field and wind-tunnel measurements in canopy flows. It is significantly different from the eddy structure educed over smooth walls by conditional sampling based only on ejections as a trigger. The characteristic eddy was also reconstructed by empirical orthogonal function (EOF) analysis, when only the dominant, sweep-generating head-down hairpin was recovered, prompting a re-evaluation of earlier results based on EOF analysis of wind-tunnel data. A phenomenological model is proposed to explain both the structure of the characteristic eddy and the key differences between turbulence in the canopy/RSL and the ISL above. This model suggests a new scaling length that can be used to collapse turbulence moments over vegetation canopies.

## 1. Introduction

Within the inertial sublayer (ISL) of high-Reynolds-Number rough-wall boundary layers, the mean wind profile is close to logarithmic and the log law relates the momentum flux to the mean wind gradient in a convenient form that is exploited in measurements and predictive models. When buoyancy forces are present, Monin–Obukhov similarity theory (MOST) introduces an extra length scale – the Obukhov length $L$ – allowing the log law to be extended to diabatic conditions and providing the theoretical basis for surface-layer meteorology. It has been known for a considerable time, however, that sufficiently close to a rough surface, MOST formulae must be modified to reflect changes in the character of the turbulence (Thom *et al.*

† Email address for correspondence: john.finnigan@csiro.au

1975; Raupach 1979; Chen & Schwerdtfeger 1989). These modifications are the result of fundamental changes in the turbulence structure that occur near the interface between the free flow and the porous, momentum-absorbing layer occupied by the roughness elements.

This so-called canopy layer and the region of modified turbulence above it, the roughness sublayer (RSL), have been studied most intensively in the atmospheric boundary layer over vegetation and also over urban canopies and in hydraulic flows over aquatic vegetation and gravel beds (Ghisalberti & Nepf 2002). Here we focus on horizontally uniform vegetation canopies in which the individual roughness elements – leaves, stems and branches – are much smaller than energetic eddies in the boundary layer so that a dynamically meaningful volume-averaged flow field can be defined. This allows us to represent momentum absorption in the canopy as a body force and the turbulent flow within and above the canopy as a continuum (Finnigan 2000). Furthermore, the physical scale of tall plant canopies means that a body of data with good vertical resolution is available both within and above the canopy.

Collection of these data has been motivated by many practical and theoretical problems. For logistical reasons, measurements of surface–atmosphere exchange from meteorological towers over crops or forests are often restricted to the RSL, and an understanding of its dynamics is critical to interpreting these results. See for example the international FLUXNET program, which aims to quantify carbon and energy exchange between the atmosphere and the terrestrial biosphere (Baldocchi *et al.* 2001). Numerical models of climate, weather or scalar dispersal typically use MOST formulae as their lower boundary condition, and over tall roughness elements, the lowest resolved grid points lie within the RSL so that departures from MOST have implications for predictions throughout the boundary layer (Physick & Garratt 1995; Harman & Finnigan 2007, 2008). Consequently, for many years micrometeorologists have devoted attention to the failure of MOST near rough surfaces and have produced empirical corrections (Raupach 1979, 1992; Garratt 1980, 1983; Cellier & Brunet 1992; Mölder *et al.* 1999). However, an explanation of these corrections at a fundamental level has remained elusive.

Turbulence statistics in the canopy/RSL are significantly different from those in the ISL of a rough- or smooth-wall boundary layer. Scaling of turbulence moments on distance from the wall (or from a displacement plane if the wall is rough) breaks down and is replaced by dependence on height-independent length and velocity scales related to the canopy geometry. The large energetic eddies responsible for most of the turbulent kinetic energy and transport in the canopy/RSL are significantly more coherent than eddies in the ISL. Most importantly, the turbulence is more 'efficient' at transferring momentum and scalars in the sense that a given flux is associated with a weaker mean gradient of velocity or concentration than is required in the ISL. It is these features that cause the breakdown of MOST. These differences are summarized in Appendix A. We hypothesize that that they can be ascribed to the fundamentally different eddy structures of the two layers.

A 'standard model' of the eddy structure of boundary layers over smooth wall or over rough walls above the RSL has emerged over the last few decades. It consists of a superposition of wall-attached 'head-up' hairpin vortices that generate Q2 ejection events ($u' < 0$, $w' > 0$) between the hairpin legs (Tomkins & Adrian 2003; Adrian 2007). Detailed analysis of laboratory flows, direct numerical simulations (DNSs) and large-eddy simulations (LESs) has shown that this structure can be self-sustaining (Zhou *et al.* 1999). At a different level it is implicit in the attached-eddy hypothesis

of Townsend (1976; see also Perry & Marusic 1995), which provides a basis for scaling the ISL. However, this mechanism is unable to explain the dominance of Q4 sweep events ($u' > 0$, $w' < 0$) in momentum and scalar transport just above and within rough walls and canopies. Neither can it explain the spatial configuration of near-wall sweeps over rough surfaces or the smooth transition from sweep domination near the wall to ejection domination above the RSL in rough-wall shear layers. Finally, it is inconsistent with eddy structure derived from DNSs and LESs of uniform shear layers and smooth-wall channel flows (Moin & Kim 1985; Kim & Moin 1986; Rogers & Moin 1987; Gerz, Howell & Mahrt 1994).

Finnigan & Shaw (2000) proposed a model of canopy eddy structure consisting of a family of 'head-down' hairpin vortices which generated Q4 sweep events between their legs. This structure was educed by empirical orthogonal function (EOF) analysis of two-point data obtained from a wind-tunnel simulation. The scale and coherence of these hairpins was assumed to be dictated by the mixing-layer hypothesis of Raupach, Finnigan & Brunet (1996), who proposed that canopy/RSL turbulence displayed features that were closer to those of a mixing layer than a boundary layer. However, while explaining many of the observed features of canopy/RSL flows, this model also failed to account for the transition from sweep dominance to ejection dominance as we move further from the wall.

Elucidation of the three-dimensional structure and dynamics of large eddies in canopy flows has been hampered by the difficulty of collecting multi-point data in real canopies or even in wind-tunnel models. In this study, therefore, we employ a high-resolution LES of a canopy flow. Applying conditional sampling to this database, we extract an average eddy structure that consists of superposed pairs of head-up and head-down hairpin vortices, which generate first a Q2 ejection and then a Q4 sweep as the hairpin pair convects downwind. Two symmetry-breaking mechanisms work in opposition to decide which hairpin is stronger. Close to and within the canopy, stretching by the mean shear preferentially amplifies the trailing head-down hairpin so that Q4 sweeps dominate. Further from the canopy top, blocking by the solid ground surface limits the growth of head-down hairpins, and the Q2 ejection-producing head-up hairpins dominate through the rest of the boundary layer. The hydrodynamic instability that is associated with the inflected mean-velocity profile at the canopy top accounts for the greater coherence of these eddies in comparison with those in the ISL and also suggests that the head-up and head-down hairpins are generated simultaneously as an instability mode rather than one appearing first and triggering the other. Our data are consistent with this view.

This structural model successfully explains a large set of observations from real and model canopies and changes the definition of the RSL from a layer of finite depth to a region in which a particular physical mechanism (head-down Q4 generating hairpins) dominates. This mechanism is present through the entire depth of the boundary layer, where it is responsible for Q4 sweep events, but above the RSL it is much less important than Q2 ejection generation by head-up hairpins. The model is also in accordance with eddy models derived from studies of uniform shear flows and channel flows in contrast to the 'standard model' described above, which consists entirely of head-up hairpins. We speculate that the standard-model viewpoint may have been biased by the selection of Q2 ejections as a conditional-sampling trigger. Our dual-hairpin model replaces the earlier single head-down hairpin model proposed by Finnigan & Shaw (2000) using EOF analysis, and we use this to illustrate the possible traps involved in such analysis if it is applied uncritically.

This paper is organized as follows. Necessary notation is defined in § 2; then in § 3 we introduce the LES canopy data set, and in § 4 use this as well as earlier wind-tunnel, field and simulation data to derive the space–time structure of the energy-containing eddies. In § 5 we compare the new results with structures in other shear flows and propose a phenomenological model for the eddy dynamics. Finally, in § 6 we summarize and emphasize the main conclusions.

## 2. Coordinates and averaging

We adopt the meteorological convention of right-handed Cartesian coordinates with $x$ aligned in the streamwise, $y$ in the spanwise and $z$ in the vertical direction. Corresponding velocity components are $u$, $v$ and $w$. We use vector or tensor notation as convenient with $\boldsymbol{x} \equiv \{x_1, x_2, x_3\} \equiv \{x, y, z\}$ and $\boldsymbol{u} \equiv \{u_1, u_2, u_3\} \equiv \{u, v, w\}$. Time averages are denoted by an overbar and departures therefrom by a prime; hence,

$$\overline{u}(t) = \frac{1}{T}\int_{t-T/2}^{t+T/2} u(t')\,\mathrm{d}t', \quad u_i = \bar{u}_i + u_t'. \tag{1}$$

It is impractical to account for the detailed spatial variation of velocity and scalar fields in the canopy airspace. Instead, statistics within the canopy are volume averaged over horizontal slabs of volume $V$, which exclude solid plant parts. These slabs are extensive enough to contain many canopy elements so that element-to-element variability is smoothed out but are thin enough that systematic vertical variation in canopy properties is retained.

The volume average of a scalar or vector function $\phi_j$ is defined as

$$\langle\phi_j\rangle(\boldsymbol{x}, t) = \frac{1}{V}d^3 \iiint_V \phi_j(\boldsymbol{x}+\boldsymbol{r}, t)\,d^3\boldsymbol{r}, \tag{2}$$

and local departures from the volume average are denoted by a double prime; so

$$\phi_j = \langle\phi_j\rangle + \phi_j'', \quad \overline{\phi}_j = \langle\overline{\phi}_j\rangle + \overline{\phi}_j''. \tag{3}$$

The averaging volumes are intercepted by solid foliage elements, and so the airspace in $V$ is multiply connected. In canopies of solid elements, expressions like (2) should be adjusted for the fraction of $V$ occupied by solids. This can be important in some flows such as in dense urban canopies but is a small correction that is usually ignored in vegetation canopies where the solid fraction is $O[0.01]$.

Flow statistics are formed by averaging first in time and then spatially over the volume $V$ (Raupach & Shaw 1982; Finnigan 1985; Raupach, Coppin & Legg 1986; Brunet, Finnigan & Raupach 1994; Finnigan & Shaw 2008). To compute mean statistics in a uniform, horizontally homogeneous canopy, we take $T$ much larger than the integral time scale of the turbulence, while the horizontal dimensions of the averaging volumes $V$ are much larger than the horizontal integral length scales of the turbulence. Volume averaging has two consequences. First, steady systematic spatial variations in velocity and scalar concentration can be correlated under the volume-averaging operation to form 'dispersive fluxes' which bear the same relationship to volume averaging as Reynolds fluxes do to time averaging. Hence, the kinematic stress $\tau_{ij}$ and scalar flux $f_{\chi i}$ in the canopy are written as

$$\tau_{ij} = \langle\overline{u_i}''\overline{u_j}''\rangle + \langle\overline{u_i'u_j'}\rangle \quad \text{and} \quad f_{\chi i} = \langle\overline{u_i}''\,\overline{\chi}''\rangle + \langle\overline{u_i'\chi'}\rangle, \tag{4}$$

where $\chi$ represents an arbitrary scalar. Viscous stresses and molecular diffusion are ignored, as they are much smaller than the Reynolds and dispersive terms. The very high turbulent intensities within the canopy airspace act to minimize the dispersive fluxes. Observations show that in artificial wind-tunnel-model canopies with solid, geometrically regular elements or in urban canopies, they can be of comparable magnitude to Reynolds fluxes in the lower canopy but typically only 10 % of the Reynolds fluxes in the upper canopy (Raupach *et al.* 1986; Bohm, Finnigan & Raupach 2000; Coceal *et al.* 2006). In natural vegetation canopies, they are difficult to measure but are assumed to be smaller than in artificial canopies; therefore we focus on the Reynolds fluxes in this paper.

Second, in the multiple-connected canopy airspace, differentiation and volume averaging do not commute for variables which are not constant at the interfaces between air and solid canopy elements. This is also true for differentiation with respect to time when the canopy elements are moving. As a result, source or sink terms appear in conservation equations for the volume-averaged variables. For example the sink term for momentum, $\langle \overline{F}_i \rangle$, representing the time-mean aerodynamic drag of foliage elements on the volume-averaged velocity, takes the form

$$\langle \overline{F}_i \rangle = -\frac{1}{V} \sum_{n=1}^{N} \int\!\!\int_{S_n} \overline{p} n_i \, \mathrm{d}S + \frac{\nu}{V} \sum_{n=1}^{N} \int\!\!\int_{S_n} \frac{\partial \overline{u}_i}{\partial n} \, \mathrm{d}S. \tag{5}$$

Here, $\overline{p}$ is the time-mean kinematic pressure and $\nu$ the kinematic viscosity; $S_n$ is the $n$th member of the $N$ foliage-element surfaces in the averaging volume $V$ and $n_i$ is the unit vector pointing from $S_n$ into the airspace. Hence the total drag is the sum of the pressure and viscous drags on each solid element in $V$. Full derivation of first and second-moment equations for velocity and scalars using time and volume averaging may be found in Finnigan (1985), Raupach *et al.* (1986) and Brunet *et al.* (1994).

## 3. LES of neutrally stratified canopy flow

### 3.1. *The equations and numerical implementation*

Elements from a number of previously described versions of the National Center for Atmospheric Research's (NCAR's) LES code were merged to create the LES code used here. In particular, the canopy representation presented in Patton *et al.* (2001) and Patton, Sullivan & Davis (2003) was implemented in the most recent version of NCAR's LES code (e.g. Patton, Sullivan & Moeng 2005; Sullivan & Patton 2008) which utilizes the message-passing interface to decompose the computation domain in two dimensions in order to distribute the computational load across processors.

LESs solve directly for the 'resolved' scales of motion, which are separated from the sub-filter scales (SFSs) by a spatial filter, analogous to the volume-averaging operator (2). The SFS motions are treated statistically. The NCAR LES uses pseudo-spectral methods in the horizontal and a second-order finite-difference method in the vertical. Its spatial filter consists of an explicit sharp wave cutoff in the horizontal and an implicit top-hat filter in the vertical. Application of this filter to the neutrally stratified Navier–Stokes equations in the multiply connected canopy space yields

$$\frac{\partial \widetilde{u}_i}{\partial t} + \widetilde{u}_j \frac{\partial \widetilde{u}_i}{\partial x_j} = -\frac{\partial \widetilde{P}}{\partial x_i} - \frac{\partial \widetilde{\tau}_{ij}}{\partial x_j} - \widetilde{F}_i, \tag{6}$$

where we introduce the tilde $\widetilde{()}$ to distinguish the spatial filtering used to derive the LES equations from the volume-averaging operator defined in (2). In (6), $\widetilde{P}$ is the resolved kinematic pressure and $\widetilde{\tau}_{ij} = \widetilde{u_i u_j} - \widetilde{u}_i \widetilde{u}_j$ is the SFS stress tensor, which represents the action of the unresolved SFSs of motion on the resolved velocity, $\widetilde{u}_i$. As in (4), we neglect viscous stresses. $\widetilde{\tau}_{ij}$ incorporates not just the conventional Reynolds stresses but also the 'Leonard' terms and cross-terms, which arise because spatial averaging over finite domains does not obey conventional Reynolds-averaging rules (Leonard 1974; Wyngaard 1982; Sullivan *et al.* 2003; Finnigan & Shaw 2008).

The deviatoric part of $\widetilde{\tau}_{ij}$ is estimated using a Smagorinsky-like eddy-diffusivity model (Smagorinsky 1963),

$$\tilde{\tau}_{ij} - \frac{1}{3}\tilde{\tau}_{kk}\delta_{ij} = -K_M\left(\frac{\partial \widetilde{u}_i}{\partial x_j} + \frac{\partial \widetilde{u}_j}{\partial x_i}\right) \tag{7}$$

with $K_M = C\Delta f E_s$, where $C$ is a constant. The length scale $\Delta f$ is the filter scale, $\Delta f = (3/2\Delta x \times 3/2\Delta y \times \Delta z)^{1/3}$, where $\Delta x$, $\Delta y$ and $\Delta z$ represent the LES grid resolution in the $x$, $y$ and $z$ directions. The velocity scale $E_s = (\tilde{\tau}_{kk}/2)^{1/2}$ is formed from the SFS turbulent kinetic energy, which is estimated using the canopy-induced modification of Dwyer, Patton & Shaw (1997) to the SFS turbulent-kinetic-energy model of Deardorff (1980).

Thom (1968) showed that the time-averaged pressure drag of the canopy (first term in (5)) is about three times larger than the viscous drag (second term in (5)). Therefore, following Shaw & Schumann (1992), Dwyer *et al.* (1997) and Patton *et al.* (2001), we model the total kinematic drag of the canopy as the product of a drag coefficient $C_d$, a one-sided plant area density $a$ and the square of the resolved velocity $\widetilde{u}_i$. The canopy-drag force $\widetilde{F}_i$ is three-dimensional and time dependent and is therefore written as

$$\widetilde{F}_i = C_d a\, U \widetilde{u}_i, \tag{8}$$

where $U = (\widetilde{u}_i \widetilde{u}_i)^{1/2}$ represents the resolved scalar wind speed. $\widetilde{F}_i$ is modelled as a smooth function of space, which implies that the filter scale, $\Delta f$, is large enough to remove any irregularity in the drag force caused by the heterogeneity of the foliage distribution.

We separate a mean streamwise-pressure gradient $\partial P^*/\partial x_1$ from the total three-dimensional fluctuating-pressure gradient; thus, $\partial \widetilde{P}/\partial x_i = \partial P^*/\partial x_1\, \delta_{i1} + \partial \widetilde{p}/\partial x_i$, where $\delta_{i1}$ is the Kronecker delta and $\partial \widetilde{p}/\partial x_i$ is therefore the resolved turbulent-pressure gradient. Combining all these assumptions, the final set of equations being solved can be written as

$$\frac{\partial \widetilde{u}_i}{\partial t} + \widetilde{u}_j \frac{\partial \widetilde{u}_i}{\partial x_j} = -\frac{\partial P^*}{\partial x_1}\delta_{i1} - \frac{\partial \widetilde{p}}{\partial x_i} - \frac{\partial \widetilde{\tau}_{ij}}{\partial x_j} - \widetilde{F}_i. \tag{9}$$

For the case presented here, the externally imposed pressure gradient $\partial P^*/\partial x_1$, which is uniform throughout the domain, is adjusted at every time step to maintain a constant mass flux of 6 m s$^{-1}$ through the upwind boundary.

To compute derivatives in (9), the code uses pseudo-spectral methods in the horizontal, a second-order finite-difference method in the vertical and a third-order Runge–Kutta scheme in time. To eliminate aliasing errors the sharp cutoff filter is applied to remove the highest one-third horizontal wavenumbers. Periodic boundary conditions are implemented for both horizontal directions. The upper boundary is specified as a frictionless rigid lid. A logarithmic law defines the flow between the lower

| Run | Grid points ($N_x$, $N_y$, $N_z$) | Domain size ($L_x/h$, $L_y/h$, $L_z/h$) | Canopy momentum-absorption parameter ($h\,C_d\,a$) | Drag coefficient ($C_d$) |
|---|---|---|---|---|
| A1 | 288, 144, 100 | 28.8, 14.4, 10 | 0.236 | 0.4725 |
| B1 | 576, 576, 100 | 57.6, 57.6, 10 | 0.236 | 0.4725 |
| C1 | 1024, 1024, 128 | 102.4, 102.4, 12.8 | 0.236 | 0.4725 |

TABLE 1. Parameters of the LES runs.

boundary and the first grid point above the boundary, using a specified roughness length $z_0 = 1.9 \times 10^{-4}h$, where $h$ is the canopy height.

In our LESs, a conservation equation for a passive scalar $\chi$ is solved in a way similar to that for momentum, namely

$$\frac{\partial \widetilde{\chi}}{\partial t} + \widetilde{u_i}\frac{\partial \widetilde{\chi}}{\partial x_i} = -\frac{\partial \widetilde{\tau}_{i\chi}}{\partial x_i} + \widetilde{S}_\chi \tag{10}$$

where $\widetilde{\tau}_{i\chi}$ is the SFS flux of $\widetilde{\chi}$, which is estimated assuming an SFS turbulent Schmidt number of 3 (Deardorff, 1980). The scalar source from the foliage $\widetilde{S}_\chi$ follows the formulation of Brown & Covey (1966), where an imposed and time-invariant canopy-top flux density (= 0.05 (arbitrary units) $\mathrm{s}^{-1}\,\mathrm{m}^{-1}$) decays exponentially with height according to the downward-integrated plant area density with a decay constant of 0.6. Periodic boundary conditions are imposed in the lateral directions, and zero-flux conditions are imposed at both the top and the bottom of the domain. Therefore, the volume-averaged scalar concentration increases continually in time.

### 3.2. *Parameter choices*

The LES model's canopy parameters correspond to the wind-tunnel model described by Brunet *et al.* (1994) and Finnigan & Shaw (2000) with the following difference. The $C_d$ value used in this LES study is 70 % of the $C_d$ quoted by Brunet *et al.* (1994) for wind-tunnel runs performed at a free-stream velocity of 10.2 $\mathrm{m\,s}^{-1}$. They found that because of the small diameter of their roughness elements, their wind-tunnel-model $C_d$ decreased as the Reynolds number $Re$ increased; so we have chosen a smaller value of $C_d$ to reflect the full-scale $Re$ values reproduced in the LES (table 1).

The grid resolution and domain sizes for the simulations are also presented in table 1. The parameters $L_x$, $L_y$ and $L_z$ refer respectively to the streamwise, spanwise and vertical dimensions of the computational domain. The three simulations (denoted by the names run A1, run B1 and run C1) differ only in the overall horizontal domain size. Initial results in configuration A1 displayed clear maxima and minima in streamwise-averaged $\widetilde{u_1}$ velocity, corresponding to weak streamwise vortices. The lateral wavelength of these vortices was similar to the height of the domain $L_z$. To establish whether this feature was a consequence of insufficient domain size, runs B1 and C1 were computed. These runs also exhibited lateral heterogeneity in mean velocity, although the amplitude of spanwise variations in $\widetilde{u_1}$ was reduced. Extending the computation time failed to remove these features, and we conclude that they are real features of the simulated flow.

Interestingly, despite stringent inflow conditioning, it was also impossible to completely remove weak streamwise vortices from the wind-tunnel flow described in Brunet *et al.* (1994) and Finnigan & Shaw (2000). It is well known that streamwise vortices are a pervasive instability mode of plane shear flows (e.g. Reynolds *et al.* 2007

and the references therein); so we conclude that the periodic boundary conditions in the LES, together with the ambient turbulence levels in the LES (particularly during the initialization phase), result in persistent large-scale streamwise vorticity as an intrinsic feature of the simulated flow. Except for the EOF and time-evolving characteristic eddy analysis (which were performed on run A1), all the results reported below were obtained from the large domain run, C1. For reference, run C1 required 10 restarts of 8 h each on 2048 Cray XT4 CPUs. Each restart consisted of 10 000 time steps of approximately 0.1 s; therefore the turbulence evolved over more than 2 h of simulated time.

### 3.3. *Forming mean statistics from LES output*

Before we can compare the LES data with measurements from the field or wind tunnel, we need to define the way turbulence statistics are formed from the LES output. First, the LES was run to steady state. Next, for each member of a set of realizations separated by time intervals much longer than the integral time scale, horizontally averaged moments were constructed from the local perturbations around the horizontally averaged mean. The corresponding SFS contributions were then added to the resolved scale moments. Finally the sum of resolved and SFS moments were ensemble averaged over the set of realizations.

For example the standard deviation of streamwise velocity is calculated as

$$\sigma_u(z) = \overline{\langle(\widetilde{u}(x, y, z, t) - \langle\widetilde{u}\rangle(z, t))^2 + \tilde{\tau}_{11}\rangle}^{1/2}, \tag{11}$$

where $\tilde{\tau}_{11}$ is the contribution to $u$ variance computed by the SFS model (7). The volume average operator $\langle\ \rangle$ is defined in (2), and here the volume, $V$, has horizontal dimensions spanning the entire LES domain ($L_x \times L_y$) and vertical extent of one grid unit $\Delta z$ so that within the resolution of the LES, it is equivalent to a horizontal average. The overbar represents a time average as defined in (1) with duration $T$ spanning the complete set of realizations. In order to avoid confusion between the tilde notation used in this section to denote resolved scale output from the LES and that used for measurements, from now on we will use the notation introduced in § 2 for both data derived from the LES and data from other sources. The operations used to derive composited structures from the LES output are described in § 4.

### 3.4. *Comparison with wind-tunnel results*

Turbulence moments from the LES computed using (11) are compared with the wind-tunnel data of Brunet *et al.* (1994) in figure 1(*a–c*). The wind-tunnel data correspond to the ensemble of 71 runs presented by Brunet *et al.* (1994) rather than their 'reference run', as their ensemble statistics were computed by a process that combined horizontal and time averages in a way that was equivalent to the combination of horizontal and ensemble averaging defined in (11).

The normalized mean-velocity profiles (figure 1*a*) are closely matched through the canopy and then diverge, the tunnel ratio $\langle\overline{u}\rangle/u^*$ being about 10 % higher at $z/h = 6$ (where $u^* = (-\langle\overline{u'w'}\rangle(h))^{1/2}$ is the friction velocity). This difference is primarily due to the differing outer-boundary conditions on the two flows. The LES is driven by an imposed pressure gradient, while the wind-tunnel flow has zero streamwise-pressure gradient, the momentum being supplied to the canopy by the steady entrainment of free-stream velocity into the growing wind-tunnel boundary layer. This difference is also reflected in the shear-stress profiles (figure 1*c*). Above the canopy, the LES shear-stress profile exhibits a constant slope exactly matching the imposed pressure gradient, while the wind-tunnel data show a shallow constant-stress region between

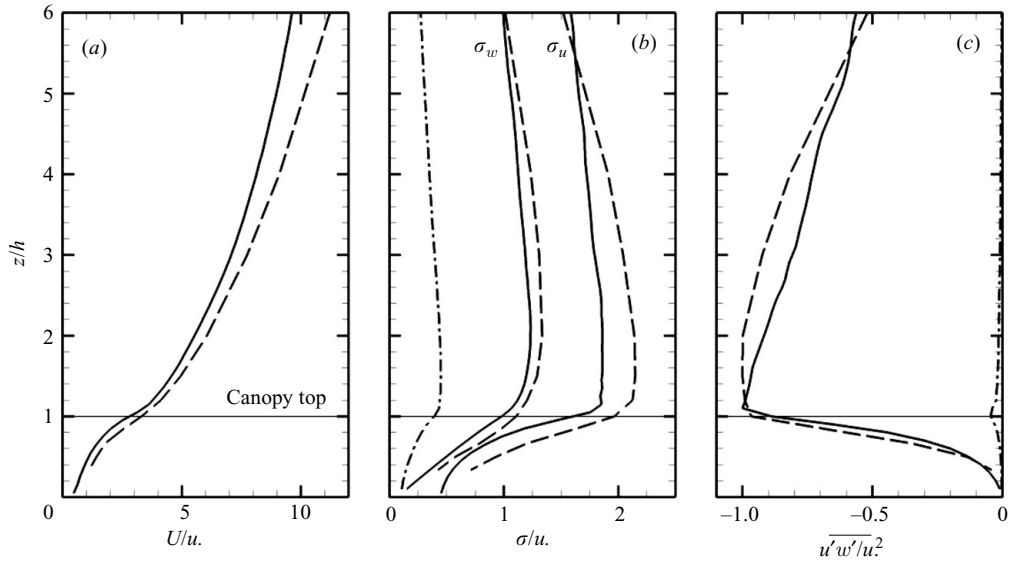


FIGURE 1. Comparison of wind-tunnel data of Brunet *et al.* (1994) and LES: dashed lines, wind tunnel; solid lines, LES. (*a*) Mean streamwise velocity, (*b*) standard deviation of the streamwise velocity $\sigma_u$ and vertical velocity $\sigma_w$ and (*c*) momentum flux. All profiles are normalized by $u_*$. The dashed–dotted lines in (*b*) and (*c*) show the SFS contribution to the LES results. The horizontal line at $z/h = 1$ depicts the canopy top.

the canopy top and $z/h = 2$. Above this height, the shear stress in the wind tunnel decreases towards zero at the outer edge of the boundary layer. Below $z/h = 6$ the two profiles differ by less than 10 %. Both $\sigma_u/u_*$ and $\sigma_w/u_*$ LES profiles (figure 1*b*) are slightly lower than the wind-tunnel data. This is most probably a result of the 70 % lower $C_d$ value used in the LES. Overall, given that the differences between the LES and wind tunnel are small, we conclude that an analysis of the eddy structure based upon the LES data is justified.

Quadrant-hole analysis of the new LES data is compared with data from four other canopies in figure 2 in the form of the ejection/sweep Q2/Q4 ratio, that is the contribution to total shear stress $\langle\overline{u'w'}\rangle$ from ejections divided by that from sweeps. We can see that the LES data follow the general pattern with the sweep contribution being dominant within the canopy and up to $z/h \simeq 1.3$ and the ejection contribution becoming increasingly more important above that level. Such behaviour is consistent with the large skewness values observed within and just above the canopy (Katul *et al.* 2006).

## 4. Eddy structure in the canopy/RSL and ISL

### 4.1. *Structure educed by compositing*

A variety of events can be used to trigger the collection of three-dimensional fields that can be ensemble averaged or 'composited' to form characteristic eddies. Zhou *et al.* (1999), in applying linear stochastic estimation to fields derived from DNS and PIV measurements, triggered on Q2 ejection events. Working with canopy-resolving LES, Watanabe (2004) used the scalar microfront that is generated ahead of a sweep as a trigger. We use the transient peaks in static pressure, which occur near the canopy top. Fitzmaurice *et al.* (2004) showed that these provide a robust indicator

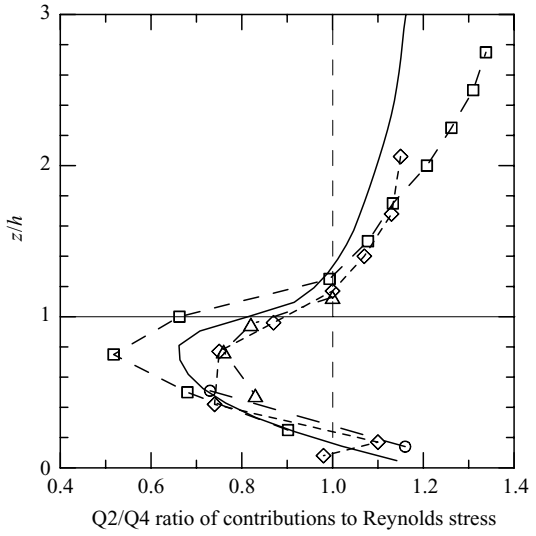


FIGURE 2. Vertical profiles of the ratio of contributions to the Reynolds stress from the ejection quadrant (Q2) and the sweep quadrant (Q4) from the LES (solid line) and from four other sources: circles, almond orchard (Baldocchi & Hutchison 1987); diamonds, cork oak plantation (Christen & Vogt 2004); triangles, wind-tunnel-model canopy (Raupach *et al.* 1986); squares, DNS of 'urban' blocks (Coceal *et al.* 2007).

of sweeps and ejections and also reliably identify scalar microfronts. Static-pressure peaks at the canopy top are associated with both Q2 ejections and Q4 sweeps so that using pressure as a trigger avoids artificial biasing of the composited flow fields towards either event.

A given number of realizations $N$ of the three-dimensional velocity, scalar and pressure fields were examined, and structures were extracted in the following manner. Regions of the $\{x, y\}$ plane at $z = h$, where the pressure trigger $p_T$ exceeded a chosen threshold $p_T = \alpha u_*^2$, were identified, and the highest pressure within this region was taken as the location of the $i$th sampling trigger $\{x_p, y_p\}_i$. Pressure peaks located within a specified horizontal distance of a larger pressure peak were discarded; $M$ pressure peaks were detected and $M$ three-dimensional volumes of the instantaneous LES perturbation velocity field were then shifted horizontally so that $\{x_p, y_p\}_i$ were coincident in a new coordinate system $\{r_x, r_y\}$, with $\{r_x, r_y\} = \{0, 0\}$ at the trigger location. Finally, the three-dimensional volumes were ensemble averaged, and the composite eddy was defined as the coherent velocity and scalar pattern surrounding the pressure trigger.

The sensitivity of the educed structure to the trigger magnitude was tested by varying $\alpha$. We found that the resulting eddy structure was independent of the trigger magnitude in the approximate range $2 > \alpha > 10$. However, we did observe that the physical size of the eddy increased somewhat with increasing trigger threshold. For this reason, we chose to impose both a minimum and a maximum pressure threshold, $p_{Tmin}$ and $p_{Tmax}$, respectively. In the examples that follow structures were extracted from $N = 18$ realizations. With $p_{Tmin} = 2\,\mathrm{m^2\,s^{-2}}$ and $p_{Tmax} = 3\,\mathrm{m^2\,s^{-2}}$ (equivalent to the minimum and maximum values of $\alpha$ equal to 4.34 and 6.51, respectively), the number of detected events $M$ was 5508.

The resulting characteristic eddy is displayed in figure 3 as a field of $\{u', w'\}$ vectors in the plane $\{r_x, 0, z\}$ and in figure 4 as fields of $\{v', w'\}$ vectors in $\{r_y, z\}$ planes

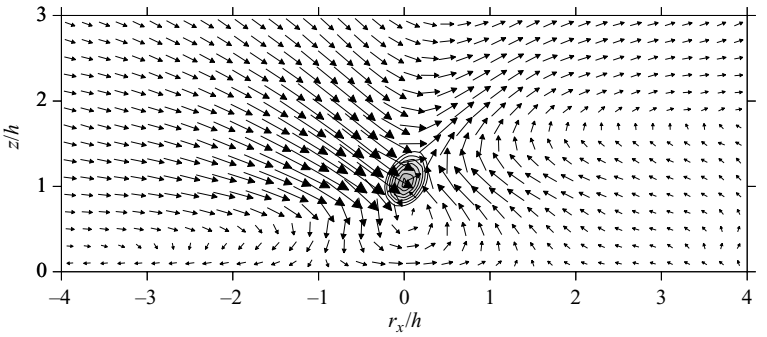


FIGURE 3. Vectors of fluctuating streamwise velocity $u'$ and vertical velocity $w'$ over an $x, z$ slice through the centre of a composite average structure identified according to minimum and maximum kinematic pressure fluctuation limits of 2 and 3 $m^2\,s^{-2}$. Maximum vector is 1.35 $m\,s^{-1}$. The contours with shading are of pressure perturbation ranging from 1.8 to 2.4 $m^2\,s^{-2}$.

at successive $r_x$ locations. We see immediately from figure 3 that on the $\{r_x, 0, z\}$ plane, the eddy consists of a coherent ejection extending from $2.5 > r_x/h > 0.5$ with maximum amplitude around $z = h$, followed by a stronger sweep extending over $0 > r_x/h > -2.5$ with its maximum amplitude just above $z = h$.

Figure 4 is more revealing. Starting at $r_x/h = -1.6$, the rearmost $\{r_y, z\}$ cross-section through the eddy, we can clearly see two counter-rotating streamwise vortices with flow towards the wall generated between them. The vortex cores are found at $r_y/h \simeq \pm 1.1,\ z/h \simeq 1.1$. As we move downwind through $r_x/h = -1.2,\ -0.8,\ -0.4$, the cores move apart such that at $r_x/h = -0.4$, they are located at $r_y/h \simeq \pm 1.7$ and move upwards to $z/h \simeq 2.2$, while the downdraft between them becomes stronger. This downdraft is blocked by the lower boundary and produces strong lateral flow in the lower canopy. This vortex pair weakens after $r_x/h = 0$, and the downdraft is replaced by an updraft. By $r_x/h = 0.8$ we can see that a new pair of vortices has emerged at a lower level, rotating in the opposite sense and generating an updraft between them. At $r_x/h = 0.8$ the vortex cores are located at $r_y/h \simeq \pm 1.05,\ z/h \simeq 0.8$. The circulation around the cores strengthens in the downstream direction. The cores retain a consistent lateral separation but become higher and by $r_x/h = 1.6$ are found at $z \simeq 1.2h$. A clear picture has emerged of two pairs of counter-rotating vortices, the downstream pair rotating in such a way as to generate an ejection and the upstream pair generating a sweep. The vortex pairs are both inclined in the $\{r_x, z\}$ plane with a slope of around 37° in the downstream direction for the sweep and about 27° for the pair associated with the ejection. The strongest sweeps and ejections are found close to the $\{r_x, 0, z\}$ plane of symmetry of the eddy, but the statistics shown in figure 2, of course, include contributions from all parts of the structure, as many coherent eddies are advected past a fixed point, blurring somewhat the dominance of strong sweeps over strong ejections.

Ideally we would like to be able to define a variable whose density surfaces reveal the three-dimensional structure of the vortices. Such a variable should reflect not only the local vorticity but also the coherent swirling nature of the structure, which is a global property. Several functions of the velocity gradient tensor $\partial u_i/\partial x_j$ have been suggested as candidates. Jeong & Hussain (1995) proposed a definition of a vortex in terms of the eigenvalues of the symmetric tensor $S^2 + \Omega^2$, where $S$ and $\Omega$ are the symmetric and antisymmetric parts of $\partial u_i/\partial x_j$. They specified a vortex core as 'a connected region with two negative eigenvalues of $S^2 + \Omega^2$' and pointed out that

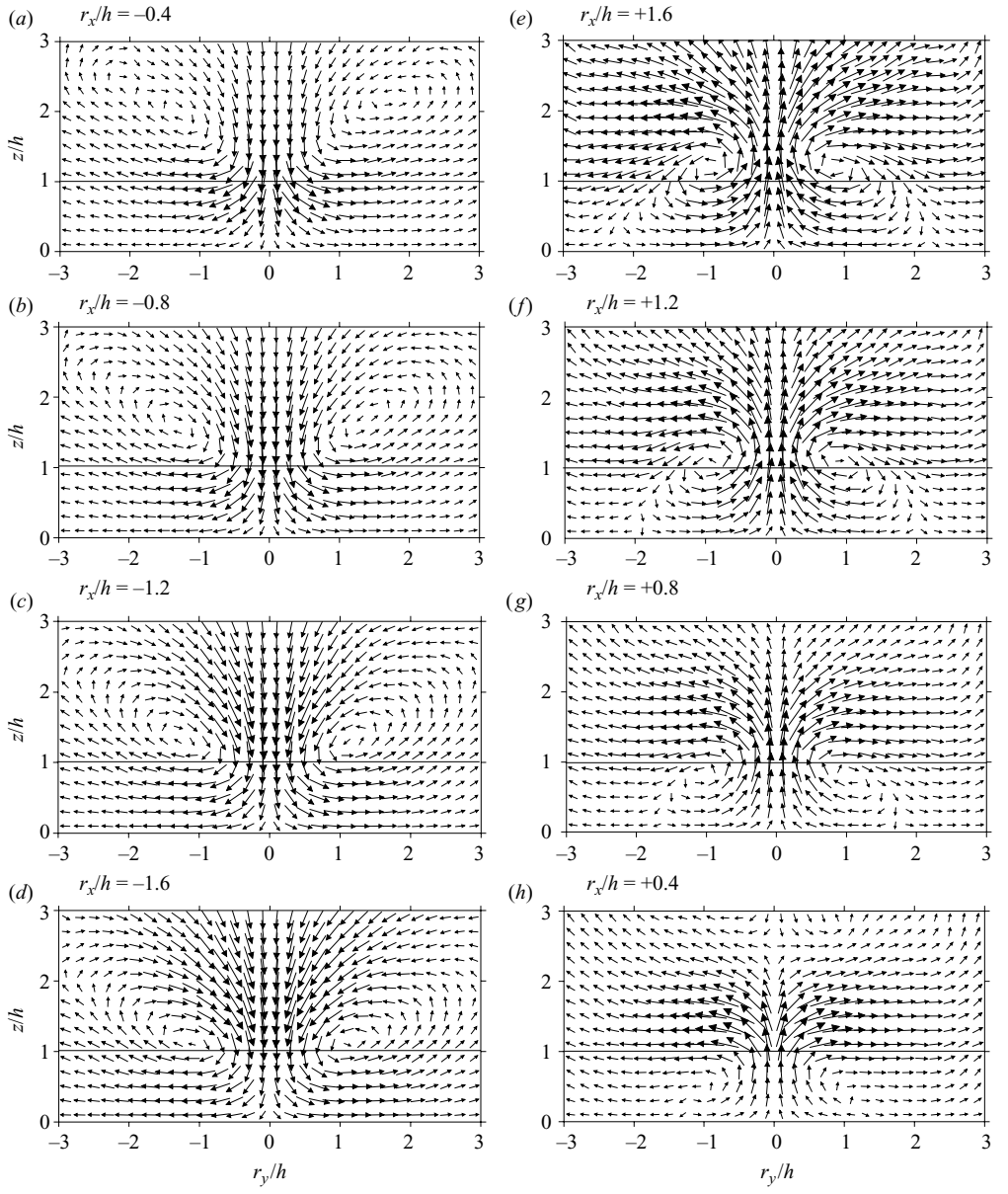


FIGURE 4. Transverse slices across a composite average structure at a series of streamwise displacements from the positive pressure peak, showing $\{v', w'\}$ velocity vectors. The left-hand series passes through the region of the sweep from the most upwind location (*d*) $r_x/h = -1.6$ (bottom left panel) to (*a*) $r_x/h = -0.4$. The right-hand series passes through the ejection from (*h*) $r_x/h = +0.4$ to the furthest downwind location at (*e*) $r_x/h = +1.6$. For clarity, vectors are not drawn to scale. Maximum arrow length is the same in each section, but the largest $\{v', w'\}$vector is found in the sweep at $r_x/h = -0.4$, and the smallest peak vector is found in the ejection at $r_x/h = +1.6$. The horizontal line at $z/h = 1$ represents the top of the canopy.

since $S^2 + \Omega^2$ is symmetric, this reduces to the requirement that the second eigenvalue $\lambda_2$ is negative. We selected a value for $\lambda_2$ by trial and error in order to visualize the vortex cores as clearly as possible. First, in figure 5, we compare contours of $\lambda_2$ with the field of $\{v', w'\}$ vectors on one of the $\{r_y, z\}$ planes of figure 4. We can see that

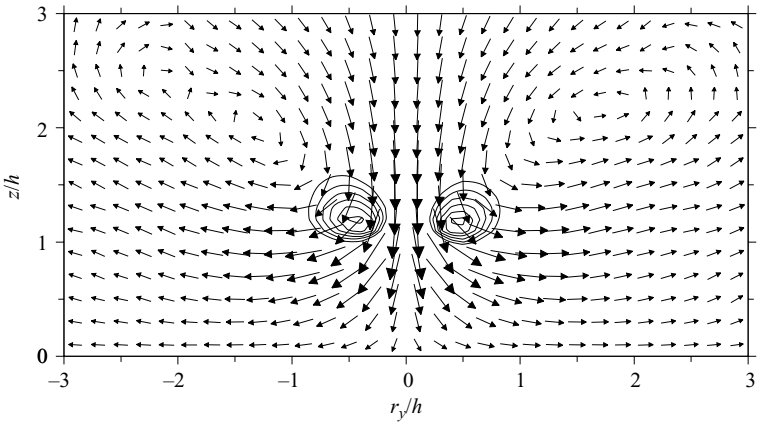


FIGURE 5. A slice across a $\{y,z\}$ plane of a composite average structure at a streamwise displacement of $r_x/h = -0.4$ near the centre of the sweep. Vectors show the $\{v', w'\}$ components of velocity, while contours are negative values of $\lambda_2$ with a peak value of approximately $-2$.

the $\lambda_2$ values are biased towards the region of high vorticity in the strongly sheared regions at the edge of the downdraft. As a result, contours of $\lambda_2$ emphasize the inner boundaries of the vortices shown in figure 5 and show a more compact structure. To avoid this mismatch we have tried other vortex identification methods, specifically the three other criteria compared to $\lambda_2$ by Chakraborty, Balachandar & Adrian (2005) ($Q$, $\Delta$ and $\lambda_{ci}$) and the eigenhelicity method of Zhang & Choudhury (2006). All of these methods, however, suffered from shortcomings the same as or more serious than $\lambda_2$, when applied to our data; so we use only the $\lambda_2$ method henceforth.

In figure 6 we present isosurfaces of $\lambda_2$ for the composite eddy, which show that the inclined streamwise vortex pairs are connected to form hairpin vortices. We see the head-up ejection-generating hairpin followed by a stronger head-down sweep-generating hairpin. Note that if we decrease the $\lambda_2$ threshold, the hairpins transform into vortex loops connected at both head and tail. This is because we are tracing perturbation rather than total vorticity, and so we should expect the vortex lines associated with the cores of the hairpins to form closed loops of perturbation vorticity (see Kim & Moin 1986, figure 4).

Head-up hairpin vortices have been directly observed in boundary layer and channel flows over many years starting with the flow visualization of Head & Bandyopadhyay (1981) and more recently by various eduction methods in real and computed flows (e.g. Kim & Moin 1986; Zhou *et al.* 1999). Head-down hairpins are observed less frequently, but in the homogeneous-shear-flow simulations of Rogers & Moin (1987) and Gerz *et al.* (1994) they occurred with frequency equal to head-ups, and in the simulations of Gerz *et al.* they appeared to be paired with head-up hairpins. They also form a key part of the flow structure associated with sweeps in the channel-flow results of Kim & Moin (1986).

Together with the two hairpins revealed by isosurfaces of $\lambda_2$, figure 6 displays isosurfaces of the contribution to the sweep and ejection quadrants of $\overline{u'w'}$ from the ensemble-averaged flow field. It is strikingly clear that the dominant contribution to the Q4 sweep quadrant is generated between the legs of the head-down hairpin, while that of the Q2 ejection quadrant is generated between the legs of the head-up hairpin. Also included in figure 6 is a visualization of the scalar microfront. This is revealed most clearly by choosing a particular value of the scalar concentration

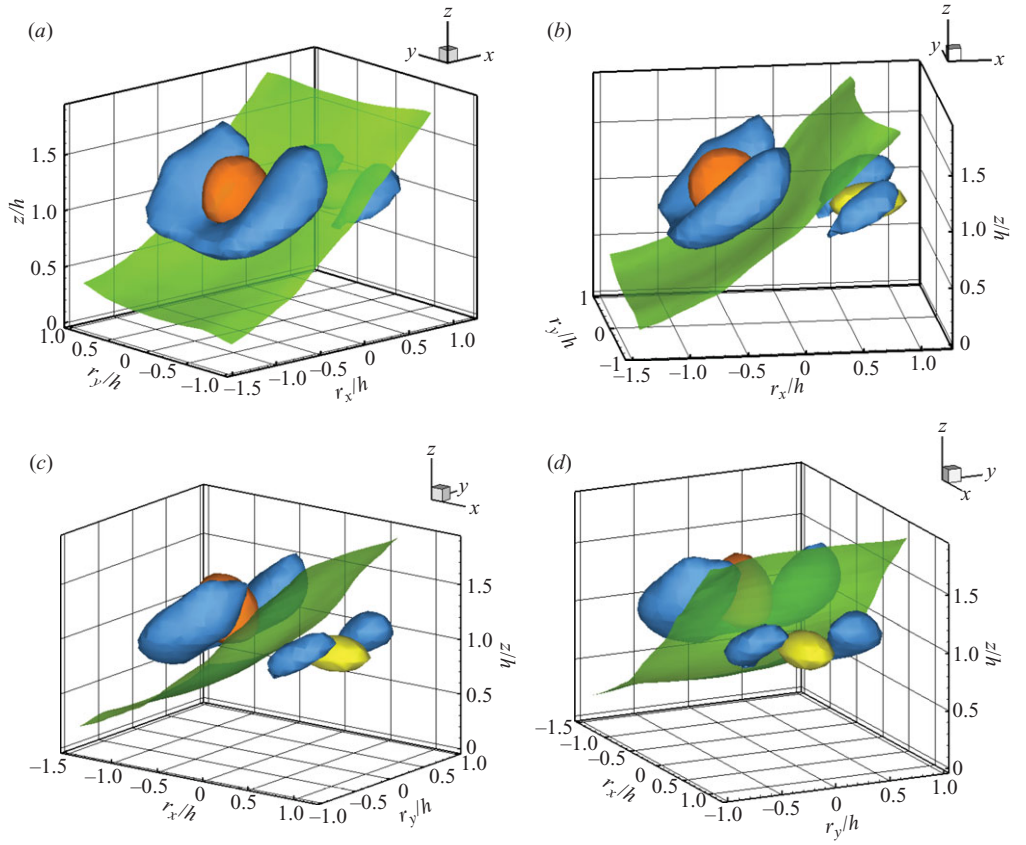


FIGURE 6. Three-dimensional representation of a structure as a composite average of a large number of events identified according to a positive pressure pulse in the vicinity of the canopy top. In this series of images, the objects rotate clockwise within the frame from (*a*) the right rear quadrant to (*d*) the right front quadrant, as shown by the coordinate system at the upper right of each part. The isosurfaces shown in blue are of $\lambda_2$ at a value of $-0.77$. The translucent sheet in green is an isosurface of zero scalar concentration perturbation from the horizontal average. The isosurface shown in orange is of $u'w'$ at a value of $-0.6\,\mathrm{m^2\,s^{-2}}$ in the region of the sweep, while that in yellow is the same quantity at a value of $-0.15\,\mathrm{m^2\,s^{-2}}$ associated with the ejection. Note that the $u'w'$ isosurface of the sweep is drawn at a value that is four times greater than that of the ejection.

close to $c' = 0$ rather than an isosurface of the gradient $\partial c/\partial x_i$. We recall that the scalar $c$ is released with constant flux density from the canopy. The coherence of the microfront is remarkable given the extremely high turbulent intensities in the canopy and illustrates the organization imposed on the flow by the large canopy eddies. It is evidently a result of the strong flow convergence between the ejection and the sweep.

An immediate question is whether the spatial relationship of the two hairpins is an artefact of our compositing process. Blocking of a sweep by the ground produces a positive pressure pulse downstream of the sweep (Shaw *et al.* 1990). Similarly, an ejection encountering faster-moving air above will produce a region of convergence and a positive pressure pulse upstream (Adrian, Meinhart & Tomkins 2000). It is possible therefore that triggering on a pressure peak aligns head-up and head-down hairpins that are spatially unrelated. We tested this by computing the conditional

probabilities of pressure peaks given following sweeps, pressure peaks given preceding ejections and pressure peaks given both following sweeps and preceding ejections. The results are tabulated in Appendix B. While the statistics depend on the magnitude of the thresholds used to identify the pressure peaks and the sweeps and ejections, it is clear that for typically 60 % of the time, a pressure peak is preceded by an ejection and followed by a sweep. This rises to 80 % if we include only the stronger sweeps and ejections.

A second set of questions concerned the temporal relationship of the events: does the sweep trigger the ejection? Does the ejection trigger the sweep? Or do the two hairpins develop simultaneously? To test this we adopted the following procedure to generate a time-evolution of an ensemble-averaged structure:

(i) The spatio-temporal locations $\{x, y, t\}_i$ of canopy-top pressure maxima were identified as individual events within 12 instantaneous three-dimensional volumes of LES output from run A1.

(ii) From each of these locations, the flow field at the canopy top was searched backwards and forwards in time and space to determine the time and place at which the pressure pulse reached its maximum amplitude. This time and space location, $\{x_p, y_p, t_p\}_i$ was taken as the centre of each event at its most mature stage. If multiple events were identified within plus or minus 20 grid points in the $x$ or $y$ direction, then only the event with the largest pressure pulse was retained.

(iii) The ensemble-averaged flow field coinciding with the pressure peaks was created by averaging all these events. Between 15 and 25 events were identified within each of the 12 independent time realizations (totalling $NT = 253$ events), and each event was shifted in horizontal space and in time so that all $\{x_p, y_p, t_p\}_i$ were coincident in a new coordinate system $\{r_x, r_y, r_t\}$ whose origin $\{r_x, r_y, r_t\} = \{0, 0, 0\}$ coincided with the ensemble maximum pressure peak.

(iv) The time-evolving ensemble-averaged flow field was created by ensemble averaging the space–time-shifted events over the time period $r_t = -12.5$ s and $r_t = +12.5$ s.

(v) The time-evolving three-dimensional ensemble-averaged eddy structure was then visualized using an appropriate $\lambda_2$ threshold.

Snapshots from the time evolution of an ensemble-averaged structure are presented in figure 7. First we note that the $\lambda_2$ isosurfaces are much noisier than those presented in figure 6. This is largely because there are many fewer events contained within this ensemble (253 compared with the $M = 5508$ events that went into computing figures 3, 4 and 6). This is a result of the extremely large storage required to perform this analysis (i.e. 250 consecutive three-dimensional volumes from 12 independent time periods, a total of 3000 three-dimensional volumes of five 8 byte variables totalling about 500 gigabytes). Second, the emergence and disappearance of the two-hairpin structure may be a poor indication of the real eddy lifetime, as destructive interference between individual eddies having different sizes, advecting at different speeds and/or having different intrinsic lifetimes may set the limit to the duration of the ensemble eddy. To the extent that this approach can resolve the question, however, it seems that the head-up and head-down hairpins appear simultaneously. Focusing on the first panel at $-6.5$ s we see that two fairly incoherent 'lumps' of $\lambda_2$ have appeared with the expected separation and inclination in the downstream direction, and by the second panel at $-1.5$ s, the two hairpin vortex shapes are clear. There is no evidence that one is triggered or induced by the other. In the last two panels we see that the stronger head-down hairpin is more persistent than the head-up, but this may be an artefact caused by the need to choose a single threshold value of $\lambda_2$ with which to

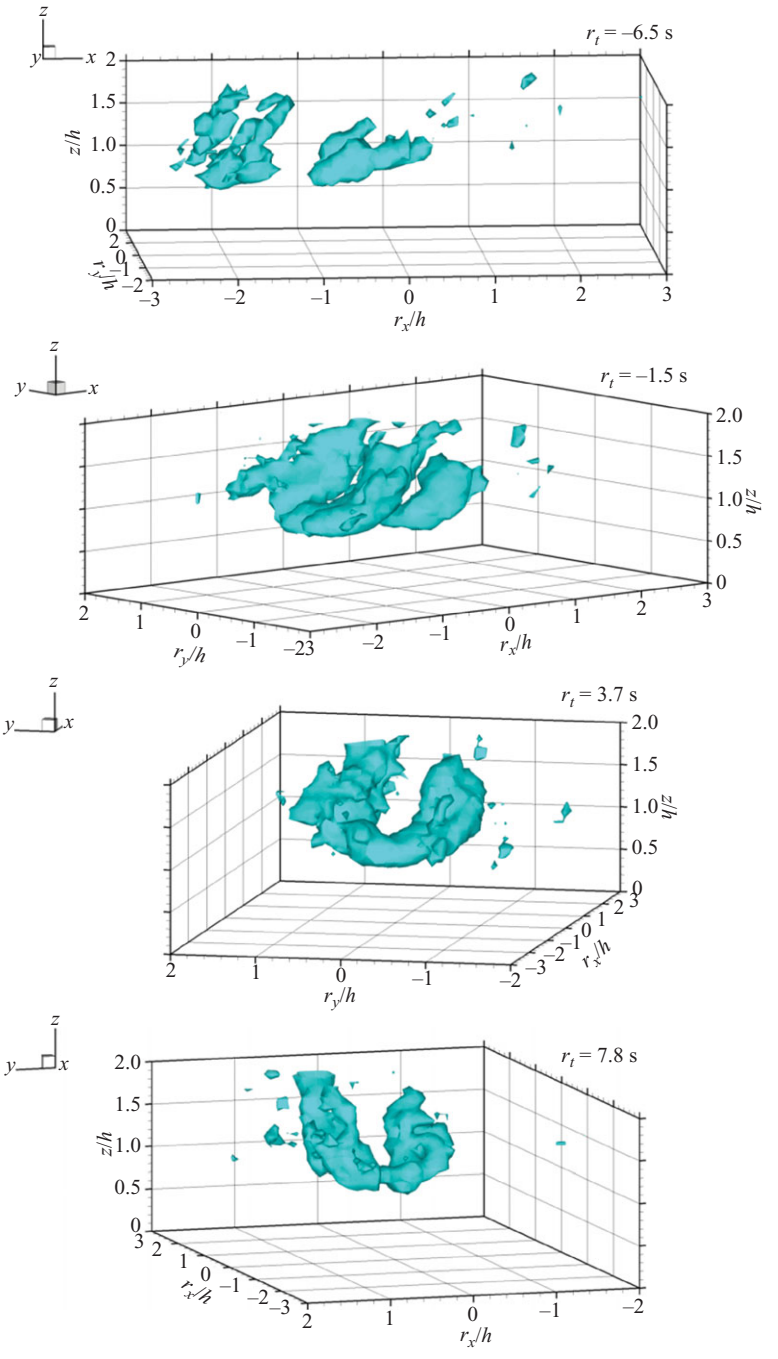


FIGURE 7. Snapshots of time evolution of the characteristic eddy as revealed by isosurfaces of $\lambda_2$. The four panels depict different times ($r_t$) and rotated views. The head-down hairpin is more coherent than the head-up in this simulation, and both hairpins are much noisier than in figure 6, as far fewer time-evolving realizations are included in the ensemble. The simultaneous appearance of both hairpins is clear.

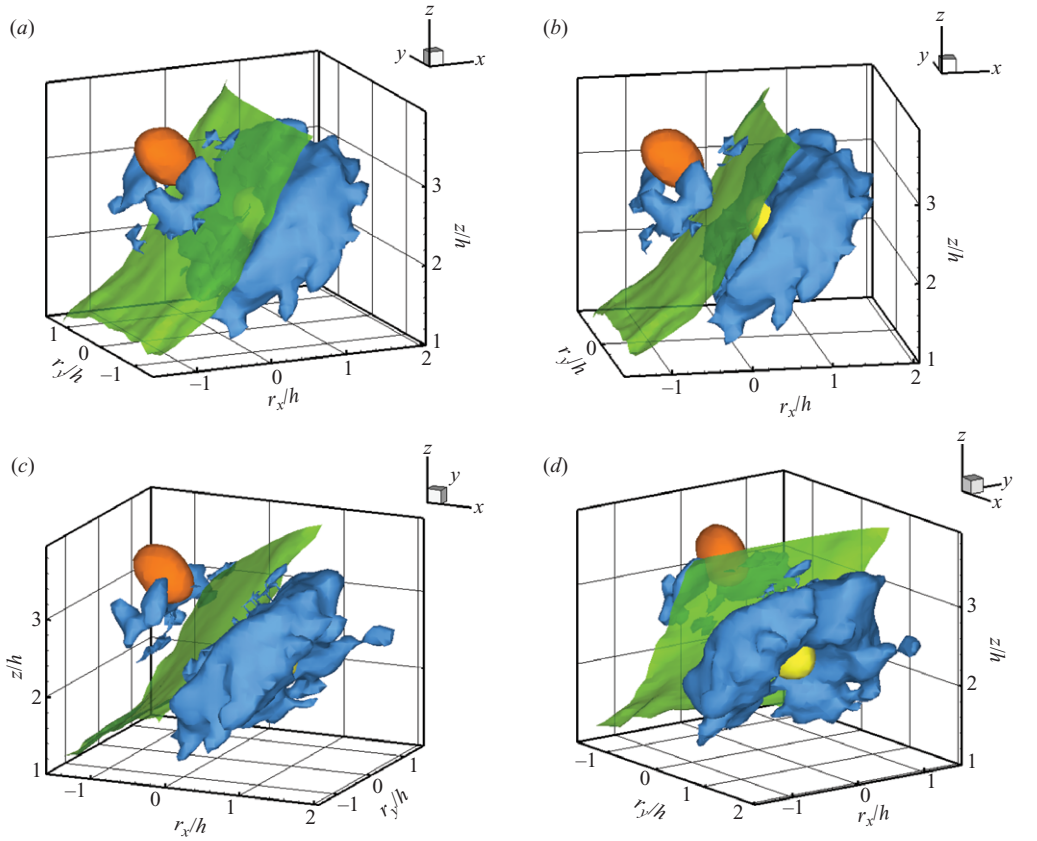


FIGURE 8. Three-dimensional representation of a structure as a composite average of a large number of events identified according to a positive pressure pulse detected at three times the height of the canopy ($3h$). In this series of images, the objects rotate clockwise within the frame from (*a*) the right rear quadrant to (*d*) the right front quadrant, as shown by the coordinate system at the upper right of each part. The isosurfaces shown in blue are of $\lambda_2$ at a value of $-0.08$. The translucent sheet in green is an isosurface of zero scalar concentration perturbation from the horizontal average. The isosurface shown in orange is of $u'w'$ in the region of the sweep, while that in yellow is the same quantity as that associated with the ejection. Note that the $u'w'$ isosurface of the ejection is drawn at a value that is 1.8 times greater than that of the ejection.

identify the structures. At a lower $\lambda_2$ value, the head-up hairpin may persist for longer in a coherent form.

In figure 8 we present a composite plot of an ensemble-averaged eddy similar to figure 6 but this time triggered on pressure peaks at $z = 3h$, which is more than four times the height above the canopy at which ejections first exceed sweeps in their contribution to $\overline{u'w'}$ (see figure 2). We can immediately see that the coherence of the eddy structure and the scalar microfront is degraded and that the head-up hairpin and its accompanying Q2 contribution greatly exceed the Q4 contribution of the weak, head-down hairpin.

This three-dimensional eddy structure successfully explains observations by a number of workers who have analysed field, wind-tunnel and numerical simulations of canopy flow. Earlier observations are summarized in Finnigan & Shaw (2000), while the more recent LES results of Fitzmaurice *et al.* (2004) and Watanabe (2004) confirm

the picture (although Watanabe's dynamical explanation of his results differs from that which we will propose in § 5). All of these data show that strong sweep motions are preceded by weaker ejections, that the sweep is preceded by lateral outflows or at least high values of $\sigma_v$ and that intense scalar microfronts are associated with the leading edge of the sweep. The structure also reveals why momentum and scalar transfer is concentrated in a narrow region elongated in the streamwise direction (Shaw *et al.* 1996; Finnigan & Shaw 2000; Su *et al.* 2000) and located between the legs of the hairpins so that the lateral extent of strong transfer is much smaller than the width of the coherent eddy.

### 4.2. *Instantaneous realizations*

To test whether the composite eddies are representative of instantaneous structures, we have looked at the flow fields of individual events that go into forming our ensemble averages. We examined plots of pressure and vertical velocity in the $\{x, y\}$ plane at $z = h$ and selected events that show a tight streamwise sequence of downdraft–pressure peak–updraft. For each event, isosurfaces of $\lambda_2$ were plotted in the hope of identifying head-up and head-down vortices. An example is shown in figure 9. To illustrate the sense of rotation, the isosurfaces of $\lambda_2$ are coloured according to whether the streamwise vorticity is positive (red) or negative (blue). In addition, an isosurface of positive pressure perturbation is shown (in green) to illustrate its positional relationship with the vortices. The isosurface of $\lambda_2$ in the example is $\lambda_2 = -10$, which is much larger than the $\lambda_2 \approx -0.77$ surfaces chosen for the composite average field. This difference is an indication of the degree of destructive interference between the individual events that go to form the composites.

Whatever threshold value of $\lambda_2$ is used to plot isosurfaces, the images are always very complicated with no clear evidence of hairpins. However, in each case, a coherent inclined vortex is seen, which could be the leg of a head-up or a head-down hairpin. Examination of a number of such instantaneous events shows, in the region upwind of the pressure maximum, a predominance of negative streamwise vorticity on the right side and positive streamwise vorticity on the left side (looking downstream). This implies a downdraft between the two legs, associated with a sweep. A clear example of this is illustrated in figure 9, although in this particular case, the region of negative vorticity appearing in blue is more extensive than that of positive vorticity. An equivalent arrangement of $\lambda_2$ surfaces and streamwise vorticity, but in reversed sense, predominates in the downwind region, associated with an ejection, although the weaker character of the ejection makes the feature less obvious.

Furthermore, figure 10 illustrates that $\{y, z\}$ cross-sections of $v'$, $w'$ vectors exhibit a tight correspondence between contours of $\lambda_2$ and the rotation centres revealed by the vectors, in contrast to what we find in the composite analyses, where $\lambda_2$ is influenced by shear, and the peak of $\lambda_2$ is displaced significantly from the visual centre of rotation as we saw in figure 5.

The failure of instantaneous snapshots to form clear hairpins corresponds to general experience when eddies are educed by velocity patterns or functions of the strain tensor, $\partial u_i/\partial x_j$ (see for example Robinson 1991; Adrian *et al.* 2000). Kim & Moin (1986) showed that identifying the vortex as a compact region of space containing parallel traces of the total vorticity vector allowed them to show instantaneous structures as connected hairpins of vorticity albeit strongly distorted by the ambient turbulence. The circulation about the cross-section of an instantaneous hairpin vortex should remain constant even as it is distorted by ambient turbulence. If the vortex cross-section increases at any point, however, due to random straining, so that the

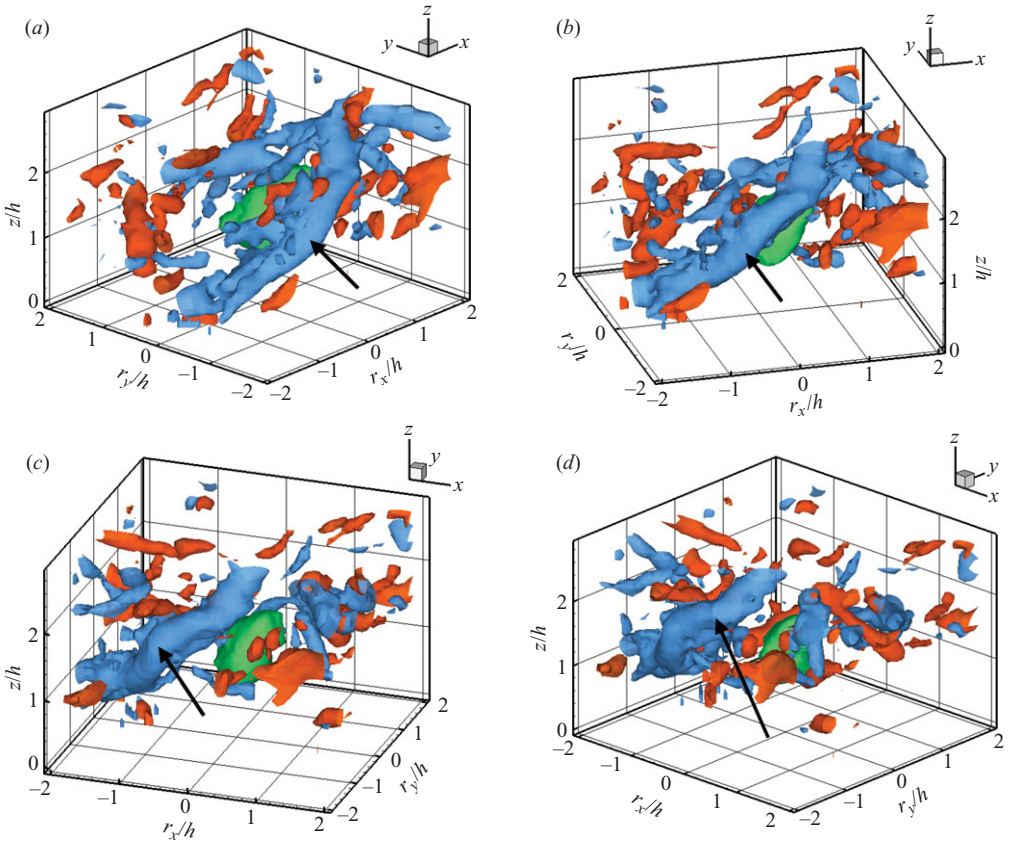


FIGURE 9. Three-dimensional representation of an instantaneous structure identified according to a positive pressure pulse in the vicinity of the canopy top and extracted from a single realization. In this series of images, the objects rotate clockwise within the frame from (*a*) the right rear quadrant to (*d*) the right front quadrant, as shown by the coordinate system at the upper right of each part. The isosurface near the centre of the domain, shown in green, is of pressure perturbation equal to approximately four times the standard deviation. Isosurfaces of $\lambda_2$ at a value of $-10$ are shown in red when the streamwise vorticity is positive and in blue when the streamwise vorticity is negative. Arrows point to the region of negative vorticity discussed in the text.

lines of vorticity that were required to keep the circulation around the hairpin axis constant occupy a greater cross-sectional area, then $\lambda_2$ might drop locally below the chosen threshold. This would give the impression of disconnected vortex tubes. This effect is exaggerated also because we are plotting perturbation rather than total velocity and (by implication) vortical structures.

### 4.3. *EOF analysis*

In analysing a wind-tunnel-model canopy data set, Finnigan & Shaw (2000) applied an approach first suggested by Lumley (1967) as a way to avoid the subjectivity of educing characteristic eddies by conditional sampling. This was to compute the EOF spectrum of the flow field. A flow field containing coherent structures has an EOF spectrum that converges significantly faster than a purely random field; so EOF analysis is a sensitive test of the presence of coherent eddies. Furthermore, with the weak assumption that coherent eddies are spatially compact, it is possible to

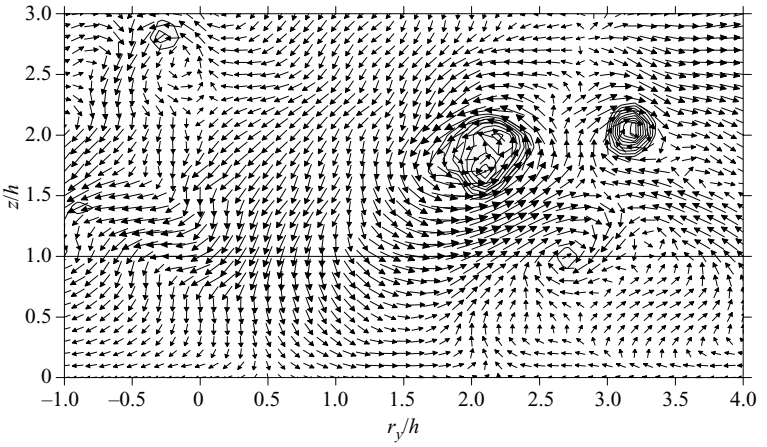


FIGURE 10. Transverse $\{y,z\}$ slice through an instantaneous realization at $r_x = -h$, upwind of a canopy-top pressure peak, showing vectors of $\{v', w'\}$ and contours of $\lambda_2$. Peak negative value of $\lambda_2$ is $-110$.

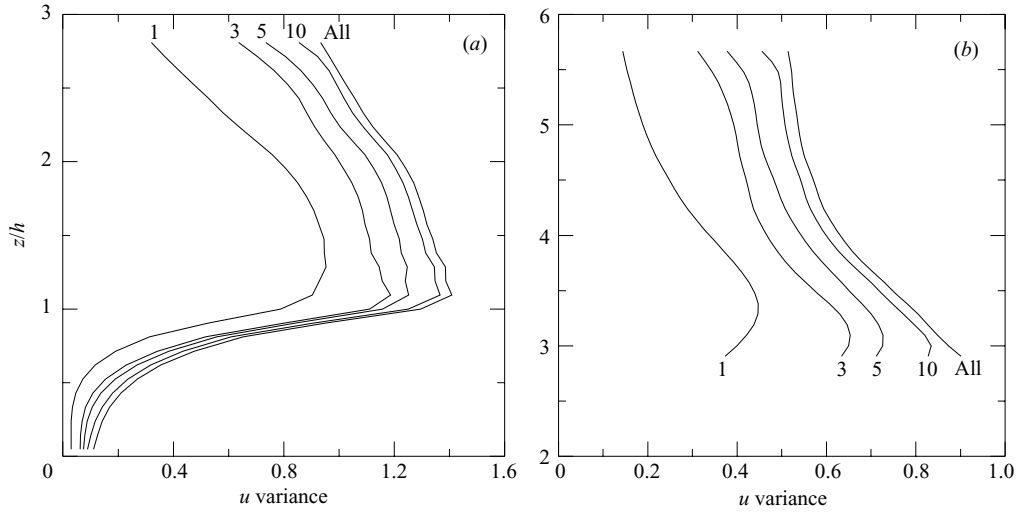


FIGURE 11. Vertical profiles of the variance of the $u$ velocity reconstructed from the sum of the first eigenmode, from the first 3, 5 and 10 eigenmodes and from the sum of all 90 eigenmodes for ($a$) the RSL (nominally $z = 0$ to $3h$) and ($b$) the ISL (nominally $z = 3h$–$6h$). The variance is calculated as the sum over all wavenumbers $k_x$ and $k_y$.

reconstruct the three-dimensional velocity (or five-dimensional velocity–pressure–scalar) field of the characteristic eddy by truncating the EOF spectrum and retaining only those eigenmodes responsible for most of the turbulent kinetic energy or variance. Finnigan & Shaw (2000) closely followed the methodology developed by Moin & Moser (1989). The same analysis has here been applied to the five-dimensional data fields from the LES. For full details of the approach, see Finnigan & Shaw (2000) and the references therein.

In figure 11 we illustrate the more rapid convergence of the EOF spectrum in the canopy/RSL region relative to the ISL by comparing partial sums of the EOF

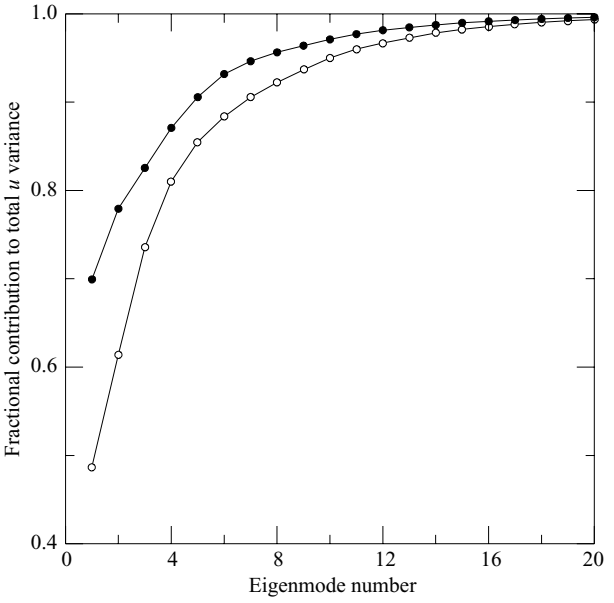


FIGURE 12. Fractional contribution to total $u$ variance from the sums of the first 1, 2, 3, ..., 20 eigenmodes. The upper curve with solid circles is for $z = 1.5h$ representing the RSL ($z = 0$–$3h$), while the lower curve with open circles is for $z = 4.5h$ representing the inertial layer ($z = 3h$–$6h$). The total number of eigenmodes in each case is 90 (30 vertical grid intervals multiplied by three variables, $u$, $v$, $w$). The variance is calculated as the sum over all wavenumbers $k_x$ and $k_y$.

eigenmodes to the total variance of $u$ velocity, in the same way as in figure 4 of Finnigan & Shaw (2000). The rate at which the $u$ variance approaches the total variance as the eigenmodes are summed is shown more clearly in figure 12, where in the RSL, the first eigenmode accounts for 70 % of the total variance, while in the ISL, the first eigenmode accounts for less than 50 %. The rate of convergence is somewhat slower than that found by Finnigan & Shaw (2000) from their two-dimensional wind-tunnel velocity fields because higher-dimensional EOFs converge more slowly than the lower-dimensional ones. The present analysis nevertheless confirms the earlier result.

We have applied the compactness condition used by Finnigan & Shaw (2000) to construct the three-dimensional velocity field of the characteristic eddy by using just the first three eigenmodes of the EOF spectrum. These three eigenmodes carry 77 % of the turbulent kinetic energy of the LES model flow. The resulting eddy is visualized using isosurfaces of $\lambda_2$ in figure 13. What we see is very similar to the head-down hairpin of figure 6 with the difference that the transverse part of the structure is weaker. Reducing the visualization threshold for $\lambda_2$ causes the transverse vortex linking the legs to appear but at the expense of more noise. This corresponds to the eddy structure educed from wind-tunnel data by Finnigan & Shaw (2000), where it was identified as a sweep-generating vortex pair. How ever, EOFs are the eigenmodes of the two-point velocity covariance tensor $\boldsymbol{R}_{ij}(x_k, x_l) = \overline{u_i'(x_k)u_j'(x_l)}$, and since $\boldsymbol{R}_{ij}$ is invariant if the signs of $u_i'$ and $u_j'$ are exchanged, the contributions of a characteristic eddy constructed from EOF modes to the Q2 or Q4 quadrant cannot be distinguished. Another way of saying this is that we cannot tell which way the legs of a vortex pair constructed from EOF modes are rotating.

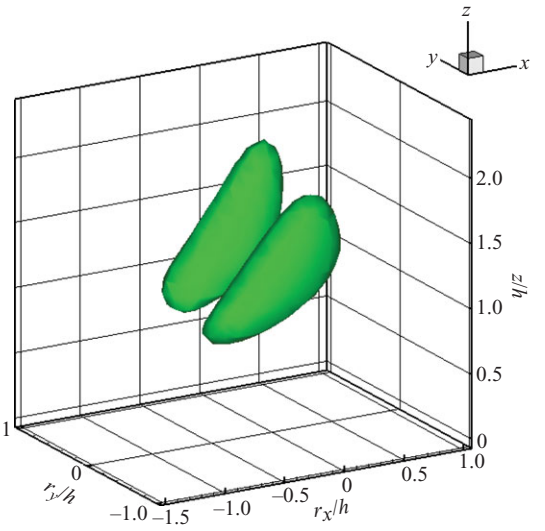


FIGURE 13. Representation of $\lambda_2$ analysis of the characteristic eddy reconstructed from LES output using the proper orthogonal decomposition of Lumley (1967) and applying the compactness condition. Only the first three eigenmodes (which are responsible for 77 % of the turbulent kinetic energy) are used in the reconstruction of the eddy.

Finnigan & Shaw (2000) deduced the direction of rotation of their vortex pair by the fact that the sweep quadrant was dominant. We can now see that the contribution of both the head-up and head-down hairpins to $\boldsymbol{R}_{ij}$ must be of the same sign, so that the EOF compactness condition superimposes their two fields, giving us a single vortex pair of indeterminate rotation as a characteristic eddy. A series of authors have presented eddy structures based on this procedure in both free and wall-bounded flows (see for example Holmes, Lumley & Berkooz 1996), and the discrepancy we see here between EOF and composite structures suggests that some of these results might bear re-examination.

## 5. Discussion

### 5.1. *Comparison with eddy structure in other shear flows*

It is instructive to summarize the available data on three-dimensional eddy structure in other shear flows to set our results in context. We will consider plane mixing layers, homogeneous-shear flows and smooth-wall channel and boundary-layer flows, where the three-dimensional structure has been educed directly.

The DNSs of plane mixing layers by Moser & Rogers (1993) and Rogers & Moser (1994) provide the most detailed information on eddy structure in such flows, although flow visualization of transverse vortices in mixing layers provided some of the earliest evidence of coherent structures in turbulent flows (e.g. Brown & Roshko 1974). At an early stage of development, the mixing layers are dominated by spanwise roller vortices which pair stochastically as the layer develops. Quasi-streamwise 'rib vortices' develop in the strongly strained braid regions between the rollers, and these vortices also pair to form coherent rib vortices with a preferred spanwise spacing. Interestingly, in these numerical simulations it was found that the development of clean rib vortices required low levels of ambient turbulence. The initial stages of kinking of spanwise

rollers and the development of streamwise rib vortices is quite well described by linear stability theory (Pierrehumbert & Widnall 1982; Liu 1988). Depending on the starting point chosen, the rib vortices and the transverse rollers can be interpreted as head-up or head-down hairpins.

Rogers & Moin (1987) computed instantaneous vorticity fields from a DNS of homogeneous-shear flow at moderate Reynolds number. They observed both head-up and head-down hairpins aligned with the direction of maximum positive strain of the plane shear, $\pm 45^{\circ}$. Head-up and head-down hairpins seemed to occur with equal frequency. Gerz *et al.* (1994) performed a similar study augmented by the addition of a mean scalar gradient to the flow so that the simultaneous development of the velocity and scalar fields could be observed. They also found an equal frequency of head-up and head-down structures but noted in addition that they tended to occur in pairs with an upstream, sweep-generating head-down overlying a downstream ejection-generating head-up. Between the two, the region of strong convergence was the location of intense scalar microfronts.

A consistent picture of the eddy structure of smooth-wall flows has been developed over the last 10 years in a series of papers by R. J. Adrian and various collaborators, using PIV measurements in real flows augmented by some numerical simulations. Their conceptual view explains many earlier observations and also some of the contemporary work that it incorporates. Its key mechanism is the generation of a primary head-up hairpin in the buffer region by the upward deflection and straining of ambient spanwise vorticity. The ejection generated between the legs of this primary hairpin generates a secondary head-up hairpin upwind, and this in turn generates another, and so on. The merging of these ejections results in a low-speed streak straddled by a sequence or 'packet' of head-up hairpins. A further head-up hairpin can be generated downwind of the primary. This mechanism has been demonstrated numerically by Zhou *et al.* (1999) and physically, albeit in a laminar flow, by Haidari & Smith (1994).

This vortex packet grows up into the ISL within an envelope inclined at around $15^{\circ}$ to the wall, although the inclination angle of the individual hairpins is closer to $45^{\circ}$. In the outer region above the ISL, the vortex packets can become detached from the wall (Adrian *et al.* 2000). Lateral-scale growth of the vortices occurs as they age but not in the self-similar way required by logarithmic ISL scaling. Instead this is accomplished by stochastic pairing of adjacent hairpins and cancellation of the oppositely signed vorticity of adjacent legs. Linear-scale growth through the ISL therefore occurs in a mean sense (Tomkins & Adrian 2003). Within the bottom of the buffer region and in the viscous sublayer, the trailing legs of the hairpins are almost parallel to the wall, being inclined at $\sim 10^{\circ}$ in the $\{x\text{–}z\}$ plane (Jeong *et al.* 1997). In this model, Q2 ejections induced between the legs of the head-up hairpins are the dominant contribution to $\langle \overline{u'w'} \rangle$ within and above the buffer region; Q4 sweeps are generated by the transverse rollers that comprise the connecting heads of the head-up hairpins. Indeed, a good deal of the evidence for the head-up hairpins in the ISL and outer region is obtained by detecting spanwise rollers in PIV slices in the $x$–$z$ plane (Adrian *et al.* 2000; Christensen & Adrian 2001).

A significantly different conceptual model is provided by the analysis of an LES of channel flow by Moin & Kim (1985) and Kim & Moin (1986). They produced ensemble-averaged three-dimensional vorticity fields by triggering on regions of deceleration into and acceleration out of low streamwise velocity, i.e. $u' < 0,\ \partial u'/\partial x < 0$ or $u' < 0,\ \partial u'/\partial x > 0$. Very close to the wall, $y^+ < 20$, there were no vortical structures, but in the ISL, $300 > y^+ > 50$, a clear pattern of head-up

followed by head-down hairpins was detected with the head-downs appearing to lie above the head-ups as in our canopy/RSL data set. Modifying the detection scheme so that the sampling trigger was a Q2 ejection removed the head-down hairpins, and similarly, triggering on Q4 sweeps removed the head-ups.

Kim & Moin (1986) were also able to extract instantaneous structures as coherent bundles of vortex lines and so showed that the ensemble-averaged hairpins were composed of strongly distorted and asymmetrical hairpin or horseshoe structures rather than 'walking sticks' or 'cane' vortices that had been fortuitously assembled into hairpins by the ensemble-averaging process as suggested by other authors (e.g. Robinson 1991; Adrian *et al.* 2000). The results of Kim & Moin (1986) give strong support to a dynamical process whereby the hairpins are generated by deflection of sheets of ambient spanwise vorticity towards or away from the wall and where the dominant sweep-generating mechanism is the same as the ejection mechanism, that is induced flow between the hairpin legs, rather than downwash in front of the head roller of a head-up hairpin.

There are clearly significant differences between the picture of eddy structure in mixing layers and homogeneous-shear flows and in channel flows according to Kim & Moin (1986) and that proposed by Adrian and collaborators. The free-shear and homogeneous-shear flows have equal probabilities of head-up and head-down hairpins, often linked in pairs, while in the channel flow of Kim & Moin (1986) both are found within the buffer and ISLs, again with a strong indication that they occur in pairs. In the conceptual model of Adrian and collaborators, in contrast, head-down hairpins play no dynamic role, and both Q2 ejections and Q4 sweeps are generated by different parts of a population of head-up hairpins. This physical picture maps directly on to the conceptual picture of the attached-eddy hypothesis introduced by Townsend (1976) and developed by Perry & Marusic (1995) amongst others and the influential flow visualizations of Head & Bandyopadhyay (1981).

It is beyond the scope of this paper to reconcile these alternative views, but a few comments may be apposite. In the analysis of Kim & Moin (1986), triggering on Q2 (Q4) events yielded only head-up (head-down) hairpins, suggesting that conditional-sampling schemes that use only ejections as triggers may exclude head-down hairpins from the resulting ensemble structures. Most of the eduction schemes used by Adrian and collaborators assume *a priori* that the coherent structures are composed of head-up hairpins. For example Adrian *et al.* (2000) and Christensen & Adrian (2001) identified transverse vortices in the $\{x, z\}$ plane as the heads of head-up rather than the feet of head-down hairpins, while Tomkins & Adrian (2003) paired localized regions of rotation in the $\{x, y\}$ plane so as to form the legs of head-up rather than head-down hairpins. Similarly, Liu, Adrian & Hanratty (2001) formed three-dimensional structures from a truncated EOF spectrum in which, as we have noted in §4.3, the dominant structure will be the only one to emerge. Finnigan & Shaw (2000), for example, found only a head-down sweep-generating hairpin because this was more energetic than the coexisting head-up, and we would expect the converse to occur where ejections dominated.

### 5.2. *A phenomenological model of canopy/RSL dynamics*

A conceptual model of the eddy structure in the canopy/RSL must explain the key differences between turbulence statistics there and in the ISL above or in the buffer layer and ISL of a smooth-wall flow. In particular we need to explain the greater eddy coherence or scale selection in the RSL/canopy, the greater efficiency of transport and the dominance of sweeps over ejections, Q2/Q4 $< 1$, changing smoothly to

Q2/Q4 > 1 as the RSL is traversed (figure 2). Our starting point is to assume that greater eddy coherence provides a sufficient explanation for the greater efficiency of turbulent transport as the canopy top is approached as seen both in an increase in $|r_{uw}| = \overline{u'w'}/(\sigma_u \sigma_u)$ and mean gradients of wind speed and in scalars that are smaller than logarithmic in the constant flux region.

The mixing-layer analogy advanced by Raupach *et al.* (1996) makes the primary cause of the coherent eddy structure in the RSL/canopy layer an inviscid instability of the inflected mean-velocity profile at the canopy top. An inflection point in the mean-velocity profile is inevitable when momentum is absorbed over a finite-height range rather than at a plane wall. Linear and nonlinear stability analysis of this inflected profile predicts a sequence of unstable eigenmodes first in two and then in three dimensions (Michalke 1964, 1965; Stuart 1967; Drazin & Reid 1981). The initial linear instability is a Kelvin–Helmholtz wave, which can be interpreted as regions of positive and negative perturbations in spanwise vorticity, alternating in the streamwise direction with a wavelength $\lambda$ that is proportional to the vorticity thickness $\delta_\omega$. In flow through a sufficiently dense canopy we assume $\delta_\omega = 2U(h)/[\partial U/\partial z](h)$, where the location of the inflection point defines $h$, the canopy top (Raupach *et al.* 1996). The background flow with this wave-like perturbation superposed is itself unstable, and a nonlinear analysis shows that the vorticity wave can evolve into finite-amplitude transverse vortices, which are spaced in the streamwise direction with the original wavelength $\lambda$ (Stuart 1967).

Identifying $\lambda$ with the streamwise separation of distinct large eddies at the canopy top, Raupach *et al.* (1996) obtained a good linear relationship, $\lambda \simeq 4.0\delta_\omega$, over a range of canopies with heights ranging from 50 mm (wind-tunnel models) to 24 m (deciduous forests). This is midway in the range $5.0\delta_\omega > \lambda > 3.5\delta_\omega$ found from DNS models and direct measurements of fully developed turbulent mixing layers but smaller than the fastest growing mode predicted by linear stability analysis of a laminar mixing layer, which is $\lambda \cong 7.0\delta_\omega$ (Michalke 1964, 1965). Despite this discrepancy, it was evident that the hydrodynamic instability associated with the inflection point results in strong scale selection for the primary streamwise mode. A feature of this instability mechanism is that the growth rate of the primary Kelvin–Helmholtz mode is proportional to the mean shear. Hence, Raupach *et al.* (1996) proposed that these coherent vortex structures should emerge preferentially when the canopy-top shear was augmented by the passage of a large-scale sweep originating in the outer part of the boundary layer. Evidence for this is the enhanced convection velocity of coherent canopy eddies, which is typically $\sim 1.8U(h)$ (Shaw *et al.* 1995; Su *et al.* 2000).

We must next explain the strong preference for the occurrence of head-up and head-down hairpins in pairs with head-downs following and overlying head-ups. Two possibilities can be considered. The first is that a random head-down deflection generates a downstream sweep, whereupon blocking by the wall produces a positive pressure perturbation. This in turn produces a velocity excursion away from the wall and eventually a head-up hairpin downstream of the sweep. Alternatively, a random head-up deflection produces an ejection which blocks the higher-velocity fluid above, producing a positive pressure perturbation. This forces a negative velocity excursion upstream and eventually a head-down hairpin upstream.

While neither of these mechanisms can be definitively ruled out, the modelling of Jeong *et al.* (1997) suggests that the latter mechanism would produce another head-up hairpin rather than a head-down, while the former requires the close proximity of the wall in order for the sweep to generate an outward excursion ahead of it. However, the key characteristics of canopy/RSL turbulence are seen even in canopies in which

a dense crown space is elevated far from the surface, as in a tropical rainforest. There the sweep cannot be strongly blocked by the ground surface. A similar observation can be made about the head-up, head down pairing observed in the homogeneous-shear simulations of Gerz *et al.* (1994). Both of the mechanisms suggested above imply a clear sequence in which one hairpin is formed before the other. As discussed in § 4.1, as far as we can tell from space–time ensemble averaging, the head-up and head-down hairpins form simultaneously, although it must be admitted that this technique is not a strong discriminator.

An alternative mechanism is suggested by the linear stability analysis of Pierrehumbert & Widnall (1982). They investigated the stability of a background flow comprising a train of 'Stuart' vortices embedded in a hyperbolic-tangent mean-shear flow. The spanwise vortex cores were located at $z = 0$ with a streamwise spacing of $\lambda$. They described two unstable modes in detail, and the first, 'helical-pairing' mode is relevant to our observations. This mode results in adjacent Stuart vortices approaching and rotating around each other. The nature of this instability is easy to understand. If all the vortices remained a distance $\lambda$ apart, then the upward displacement of a vortex in the induced velocity field of its downstream neighbour is exactly cancelled by the downward displacement generated by its upstream neighbour. If two vortices approach more closely than $\lambda$, however, the effect of their mutually induced velocity fields causes them to rotate around each other in a clockwise sense, the downwind vortex being deflected below $z = 0$ and the upwind one above $z = 0$. This vortex-pairing instability was described in two-dimensional mixing layers by Winant & Browand (1974) and shown to be the primary mechanism of transverse growth of the mixing layer. It has also been clearly observed in two-dimensional flow above a canopy in a water channel (White & Nepf 2007).

Pierrehumbert & Widnall (1982) showed that the growth rate of this mode is largest when the Stuart vortices remain parallel to the spanwise $y$ axis, but this is itself an impossibly unstable configuration, and two vortices will initially be caused to approach closer than $\lambda$ by ambient turbulent perturbations of finite spanwise extent. If two Stuart vortices are caused to approach closer than $\lambda$ at some $y$ position by a random turbulent fluctuation, then their upstream and downstream neighbour pairs will also suffer an imbalance in their induced motions and will also commence to rotate around each other, and in this way a streamwise train of vortex pairings centred on the same $y$ location will propagate upwind and downwind. Hence, Pierrehumbert & Widnall (1982) showed that the most probable helical-pairing mode is periodic in $y$ with a period $2\lambda/3$ and in $x$ with a period $2\lambda$. This pattern is displayed in figure 6 of Pierrehumbert & Widnall (1982), and it is clear that with one choice of origin, the pattern can be interpreted as a series of head-down hairpins overlying head-ups or, if we shift the origin laterally by half a period, as a series of the head-ups overlying head-downs. If this instability is the origin of the twin-hairpin eddies we have educed, their streamwise wavelength should match the sub-harmonic helical-pairing mode with eddies having an average streamwise spacing of twice the fundamental Kelvin–Helmholtz wavelength of $\lambda \cong 7.0\delta_\omega$. At first sight, this prediction is at odds with the conclusion of Raupach *et al.* (1996), who found that their observed eddy spacing was closer to $\lambda \cong 4.0\delta_\omega$. To resolve this roughly fourfold discrepancy we revisited the calculations of Raupach *et al.* (1996) and made the following observations.

First Raupach *et al.* (1996) based their observations of $\lambda$ on measurements of the streamwise correlation in vertical velocity, $w'$, using primarily $f_{wp}$, the peak in the frequency spectrum of $w'$ and assuming Taylor's hypothesis, adjusted for the observed convection velocity of canopy-top eddies, which was taken as $U_c \simeq 1.8\langle\overline{u}\rangle(h)$

(Finnigan 1979; Shaw *et al.* 1994; Su *et al.* 2000). However, a comparison between the peak frequencies of $w'$ and $u'$ power spectra in the canopy/RSL reveals that the streamwise velocity peaks at a normalized frequency, $(f_{up}\,h)/\langle\overline{u}\rangle(h)$, which is between a quarter and a half of that of the vertical velocity (Kaimal & Finnigan 1994), so that basing the relationship between $\lambda$ and $\delta_\omega$ on $f_{up}$ rather than $f_{wp}$ brings us much closer to a match with the sub-harmonic mode.

Furthermore, the data of Shaw *et al.* (1994) and Su *et al.* (2000) reveal that streamwise integral length scales from two-point data are typically twice as large as those obtained by applying Taylor's hypothesis to single-point data. We conclude that if we adjust the results of Raupach *et al.* (1996) for the discrepancy between the streamwise correlation of $w'$ and $u'$ and also for the difference between single-point and two-point length scales, we obtain a $\lambda$ value that is consistent with the sub-harmonic mode, viz. $\lambda \simeq 15.0\,\delta_\omega$. We can also compare the spanwise spacing of the hairpin vortices ($\Delta r_y \approx \pm 1.1h$) with the streamwise extent of the composite eddy ($\Delta r_x \approx \pm 2.5h$). At $\Delta r_y/\Delta r_x \approx 2.2/5.0$ this is slightly narrower than 2/3, the most probable ratio predicted by Pierrehumbert & Widnall (1982), but is compatible with it, given the eddy has evolved well past its linear phase. We note also that the measurements of Ghisalberti & Nepf (2002) in a quasi-two-dimensional shallow-water flow over a canopy and those of White & Nepf (2007) in a truly two-dimensional canopy flow had transverse vortex wavelengths that matched the primary Kelvin–Helmholtz value of $\lambda \cong 7.0\delta_\omega$ rather than the shorter wavelength reported by Raupach *et al.* (1996). In these two cases, the flow configuration does not allow the final three-dimensional transition to coupled-hairpin eddies.

A possible sequence of instabilities leading to the development of a train of head-up and head-down hairpins is sketched in figure 14. We suggest that the well-observed sequence of instability from an initial Kelvin–Helmholtz wave to a train of coherent transverse Stuart vortices is triggered when a large-scale sweep from the outer part of the boundary layer raises the canopy-top shear above some threshold so that the instability can emerge from the background turbulent 'noise' (figure 14*a*, *b*). At some spanwise position $y_p$ this train of transverse vortices is perturbed by a random turbulent eddy, triggering the upwind and downwind propagation of helical-pairing instabilities as neighbouring vortex tubes approach and are deflected in each other's induced velocity fields at the same transverse location $y_p$. As shown in figure 14*c* the heads of the 'proto' head-up hairpins are deflected upwards and forwards by their downwind neighbours, while the tails of the proto head-down hairpins are deflected downwards and backwards by their upwind neighbours.

Finally, as the 'proto hairpins' are stretched by the mean shear, the vorticity in their legs is amplified; their relative motion in a frame moving with the hairpins is dominated by their self-induction; and the streamwise symmetry of the head-up, head-down sequence is broken. The self-induced motion of the head-up hairpin is upwards, while that of the head-down is downwards (Widnall 1975), so that a pair of a leading head-up and a trailing head-down converge to generate a region of flow convergence between them and a positive pressure pulse (figure 14*d*). In contrast the self-induced motions of a pair consisting of a leading head-down and a trailing head-up act to move them apart.

This model, particularly the last phase shown in figure 14(*c*, *d*), is highly speculative and calls for a more rigorous explanation than the one we have advanced here. For example we recall that this situation was also observed in a uniform shear flow by Gerz *et al.* (1994), so that the mechanism of hairpin pairing must be independent of the vertical heterogeneity of the mean flow and any instabilities that are associated with

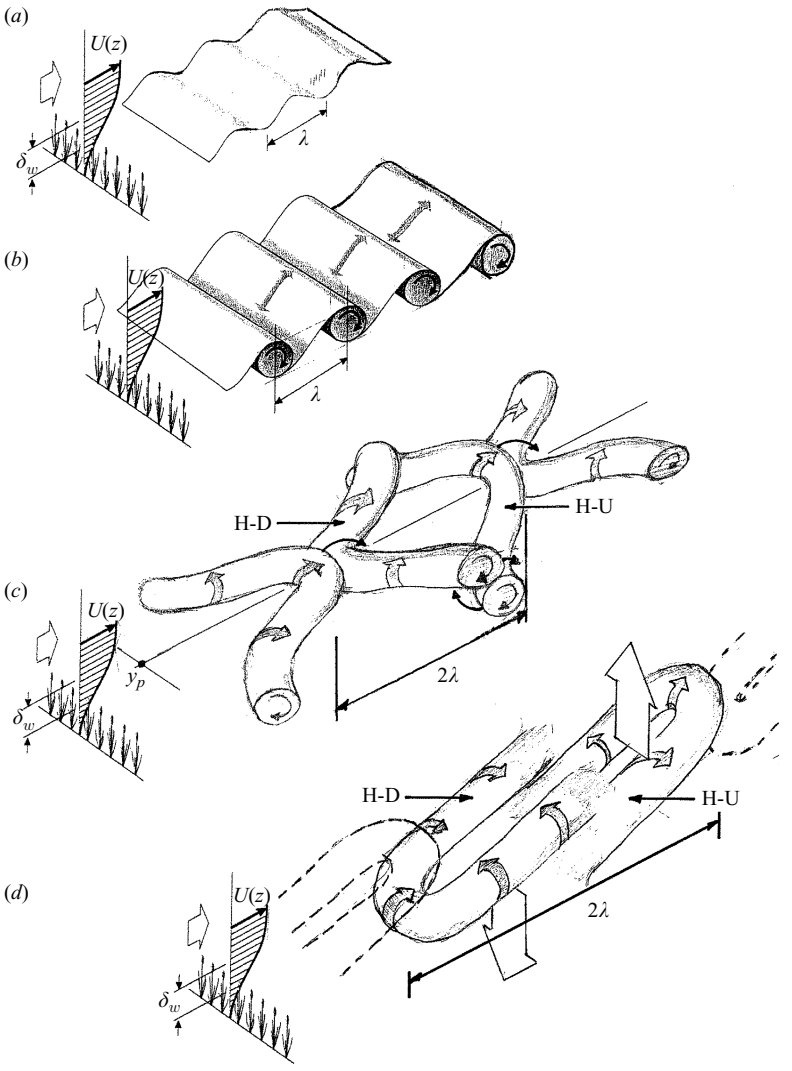


FIGURE 14. Schematic diagram of the formation of the dual-hairpin eddy. (*a*) The initial instability is a Kelvin–Helmholtz wave of wavelength $\lambda$, which develops on the inflected mean-velocity profile at the canopy top. (*b*) The resulting velocity field is nonlinearly unstable, and successive regions of alternating spanwise vorticity clump into coherent 'Stuart' vortices, which retain the wavelength, $\lambda$. (*c*) Two successive Stuart vortices are moved closer together at some spanwise location $y_p$ by the ambient turbulence. The mutual induction of their vorticity fields causes them to approach more closely and rotate around each other. Vortex pairing doubles the wavelength of the disturbance to $2\lambda$. Note that this disturbance of the streamwise symmetry of the induced velocity fields of successive vortices will propagate upwind and downwind at the same $y$ location. (*d*) As the initial hairpins are strained by the mean shear, most of the vorticity accumulates in the legs, and self-induction by the vortex legs dominates the motion of the hairpins. As a result, the head-down hairpin moves down, while the head-up hairpin moves up. The broad arrows in (*d*) indicate the direction of hairpin movement under this self-induction. Note that in (*d*) only the two central paired vortices are shown in full. It is assumed that a similar pairing process proceeds upwind and downwind.

it. We also need to emphasize that this is a model of the ensemble structure and relies heavily on the predictions of linear instability theory. This approach together with the companion approach of rapid-distortion theory has a long provenance in explaining aspects of turbulence structure (e.g. Townsend 1976; Hunt & Carruthers 1990). Liu (1988) presented a detailed justification of the application of linear theory to free-shear flows. In our case, the vortical structures obtained by compositing or EOF analysis match the predictions of stability theory surprisingly well, but individual realizations are strongly distorted around their composite averages by the ambient turbulence (figure 9). The eigenmodes predicted by stability theory should be viewed, therefore, as the preferred shapes towards which the fully turbulent flow tends (Frederiksen & Branstator, 2005). Nevertheless, these models offer a compelling explanation for the dominance of a single preferred mode shape and scale for the RSL–canopy eddies.

### 5.3. *Transverse symmetry breaking*

Head-up hairpins generate ejections, while head-down hairpins produce sweeps; so the dominance of sweeps in the RSL/canopy region and of ejections in the ISL requires some symmetry-breaking agency. There are two symmetry-breaking mechanisms at work in a wall-bounded shear flow. Above the wall, downward motions with horizontal scales comparable to the distance to the wall are effectively blocked (Hunt & Morrison 2000) so that at any $z$ location, the probability of large deflections of hairpin vortices away from the wall exceeds that of deflections towards the wall. At the same time, in a roughly logarithmic velocity profile, hairpins deflected downwards experience stronger strain and vortex amplification than hairpins deflected up by the same amount. In a canopy–boundary-layer profile this effect is amplified near the canopy top so that vortices deflected downwards are strained and rotated much more than those deflected upwards the same distance. Note that in the conceptual model advanced in § 5.2, these deflections are largely a result of self-induced motion of the hairpin vortices and strain and advection by the mean flow.

We have illustrated this asymmetry in strain rates by plotting in figure 15(*b*) $\partial^2\langle\overline{u}_1\rangle/\partial z^2$ versus $z$ from the wind-tunnel data of Brunet *et al.* (1994), which matches the LES results well as shown in figure 1. The second derivative is obtained by fitting a cubic spline to the data with the fit shown in figure 15(*a*). We can interpret the distribution of $\partial^2\langle\overline{u}_1\rangle/\partial z^2$ around $z=h$ as a measure of the rate that the shear is changing with, $z$, and therefore of the strain that a deflected vortex would experience. We see clearly in figure 15(*b*) that the shear falls much more rapidly above the canopy ($\partial^2\langle\overline{u}_1\rangle/\partial z^2 < 0$) than within it.

Above a smooth solid wall, the greater probability of large upward deflections outweighs the greater straining experienced by downward deflections, and head-up hairpins dominate the dynamics, increasingly so as we move further from the wall. At the canopy top, in contrast, the porous canopy allows downward deflections of similar amplitude to upward deflections, at least for deflections whose vertical extent is of the order of the canopy depth $h$ or smaller, so that the greater strain downward hairpins experience ensures that sweeps dominate. As we move above the canopy top and the sizes of the eddies causing deflections become larger than $h$, the presence of the wall again becomes the dominant factor so that sweep-generating head-down hairpins become less important than ejection-generating head-ups. The crossover point at which Q4 sweeps cease to make a larger contribution to momentum transfer than Q2 ejections varies with the canopy structure but appears to be a function of the vorticity thickness (see figure 2).

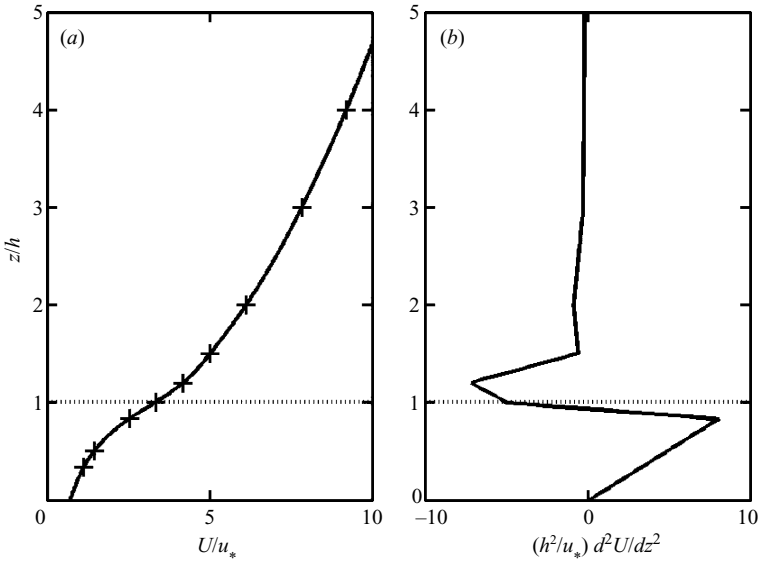


FIGURE 15. (*a*) Cubic spline fit to the wind-tunnel observations of Brunet *et al.* (1994) (crosses); (*b*) second derivative of the fitted curve from (*a*).

To summarize this conceptual model, the hydrodynamic instability associated with the inflection in mean shear at the canopy top provides both strong scale selection and a train of coherent spanwise Stuart vortices that is unstable to random turbulent perturbations. When two Stuart vortices are locally deflected towards each other, their mutual induction causes one to move up and the other to move down. Because the vortex train develops above a porous canopy layer, significant downward deflections are allowed, producing hairpins that are strained faster and whose vorticity is preferentially amplified than those deflected upwards. As straining by the mean shear amplifies the vorticity in the hairpin legs, the self-induced motion of the hairpins results in preferred pairings with a leading head-up and trailing head-down and a region of flow convergence between them. For vertical excursions much larger in scale than the canopy height, blocking by the solid surface ensures that outward excursions dominate, just as in smooth-wall flows. These two opposing symmetry-breaking mechanisms explain the shift from sweep to ejection dominance as we move up through the RSL into the ISL.

## 6. Summary and conclusions

This discussion of eddy structure in and above plant canopies has direct relevance to rough-surface flows in general. Two key features of canopy/RSL flows – the dominance of the sweep over the ejection quadrant in momentum transfer and the existence of an RSL in which momentum is transferred more 'efficiently' towards the surface than in the ISL above – are also seen over rough walls composed of bluff objects (Bohm *et al.* 2000; Coceal *et al.* 2007). The rich data sets that have been collected in and above vegetation canopies, however, as well as having intrinsic interest, allow a more detailed investigation of the underlying processes than has so far been possible over bluff surfaces.

A series of other features of the turbulence, which are summarized in Appendix A, show that the canopy/RSL turbulence is more coherent than that in the ISL and that it is dominated by energetic eddies much larger in scale than the individual elements of the vegetation. The five-dimensional velocity–pressure–scalar field of these dominant eddies has been educed by compositing data from an LES. This numerical simulation closely matches a wind-tunnel model (Brunet *et al.* 1994), which in turn displays the key features of natural vegetation canopies. The trigger used for compositing data volumes was a peak in the static-pressure fluctuation at the canopy top. Earlier analysis of field data (Gao *et al.* 1989) and LES output (Fitzmaurice *et al.* 2004) has shown that this trigger was usually coincident with scalar microfronts in canopies.

The eddy structure revealed was a linked pair of hairpin vortices, one upstream and one downstream of the pressure peak and both inclined in the downstream direction. The downstream hairpin had a head-up orientation, and the sense of rotation of the vortex legs was such as to generate a strong Q2 ejection contribution to shear stress between the legs. The upstream hairpin partly overlaid the downstream, and it had a head-down orientation with an opposite sense of rotation; so a strong Q4 sweep event was generated between its legs. The convergence between the sweep and ejection produces both the static-pressure pulse and an intense and coherent scalar microfront lying between the two hairpins (see figures 3, 4 and 6).

This two-hairpin structure is different from that derived by EOF analysis of this data set or of the prototype wind-tunnel data set by Finnigan & Shaw (2000). In both of those cases a compactness condition was used to restore the inter-eigenmode phase relationships, which are lost in the EOF procedure. This compactness condition meant that the head-up and head-down hairpin vortices were superimposed, and the sense of rotation of the vortex was defined by the need to generate a Q4 sweep as the dominant shear-stress quadrant so that an eddy consisting only of a head-down hairpin was inferred incorrectly. This experience sounds a warning for the use of EOF eigenmodes in eddy reconstruction procedures in which the sense of rotation is added empirically (e.g. Holmes *et al.* 1996).

The two-hairpin eddy is also distinctly different from the eddy structure inferred by a range of conditional-sampling techniques in smooth-wall boundary-layer and channel flows in which the conditional sampling has been triggered by Q2 ejections. These approaches have produced a model for smooth-wall structure consisting of packets of head-up Q2 ejection-generating hairpins, which straddle and synergistically generate coherent low-speed streaks (e.g. Adrian *et al.* 2000). In this picture, the origin of any Q4 sweep is the transverse roll vortex that connects the two legs of the hairpin (Zhou *et al.* 1999). Above the buffer region, growth of individual hairpins and random mergers of adjacent hairpins leads to steady scale growth. Other simulations of smooth-wall channel flows, where eddy structure or coherent vortices are not selected based on the presence of ejections, show populations of both head-up and head-down hairpins. While contrasting with the picture developed in the references above, these simulations do fit well with the present data set.

Based on the properties of this dual-hairpin structure together with earlier analysis that has shown the similarities between canopy flows and plane mixing layers, we have proposed a phenomenological model to explain the unique characteristics of canopy/RSL turbulence. This model has three key features: strong scale selection by a hydrodynamic instability; competing symmetry-breaking processes, one of which dominates at the canopy top and the other at higher levels; and spatial eddy structure corresponding to the linear eigenmodes associated with the hydrodynamic instability.

Canopy/RSL eddies are much more coherent than those in the ISL, and we ascribe this to the strong selection for a single instability mode of the inflected mean-velocity profile at the canopy top. Raupach *et al.* (1996) showed a close relationship between the scale of this inflection-point shear and the resultant eddy scale over a thousand-fold size range in canopy heights. We have re-analysed the data of Raupach *et al.* (1996) and have shown that it is compatible with the dual-hairpin structure once differences between the integral length scales of vertical and streamwise velocity fluctuations are accommodated. In contrast, above smooth walls no clear scale-selection mechanism has been advanced for the observed spanwise spacing of $\sim 100 y^+$ for the streamwise vortices in the buffer and viscous sublayer (Jeong *et al.* 1997). Streamwise vortices are certainly the dominant linear instability modes of plane shear flows, but explicit parameter tuning is required to match the observed spacing (e.g. Butler & Farrell 1992).

Further indirect evidence for the fundamental role played by the hydrodynamic instability is provided by the extension of MOST to the RSL by Harman & Finnigan (2007, 2008). They used the vorticity thickness, $\delta_\omega$, as an extra scaling length and were able to match observed mean-velocity and scalar profiles in the upper canopy, through the RSL and into the ISL across a range of canopy densities and diabatic stabilities. Building on this work, we expect that $\delta_\omega$ is the appropriate length scale to collapse higher moments of velocity in the RSL/canopy layers. This will be investigated in a future publication.

Finally, we note that we have at several points highlighted the similarity between the statistics of turbulence over vegetation canopies and rough surfaces consisting of bluff objects as in urban canopies. The eddy coherence resulting from a hydrodynamic instability provides a consistent explanation in the former case. Over a canopy of bluff objects, however, it seems unlikely that the inflected velocity profile that exists when we apply horizontal averaging can play the same dynamical role that it does in vegetation, where the solid-element sizes are much smaller than the sizes of the large eddies. Discovering the equivalent mechanism in canopies of bluff objects, therefore, remains a challenging problem.

The authors would like to acknowledge the many fruitful discussions they have had with Dr Omduth Coceal, University of Reading, and Dr Ian Harman, CSIRO, and the contributions of Dr Li Fitzmaurice, Queensland Department of Natural Resources and Mines, in providing data for comparison and of Dr Peter Sullivan, NCAR, in developing much of the LES code. E. G. Patton was supported in part by the National Science Foundation's Science and Technology Center for Multi-Scale Modeling of Atmospheric Processes, managed by Colorado State University under cooperative agreement no. ATM-0425247.

## Appendix A. Velocity statistics in the canopy/RSL and ISL

The differences between turbulent statistics in the ISL and in the canopy/RSL have been comprehensively reviewed by Raupach *et al.* (1996) and Finnigan (2000). Finnigan & Shaw (2000) also presented a detailed summary of conditionally sampled statistics in these layers. Here we state the key differences:

(i) The mean-velocity profile $\langle \overline{u} \rangle(z)$ has an inflection point at the canopy top, where its vertical location can serve as a dynamic definition of the canopy height, $h$. Second moments, $\langle \overline{u'w'} \rangle$, $\langle \overline{u'^2} \rangle$, $\langle \overline{w'^2} \rangle$, are approximately constant above the canopy but decay rapidly with decreasing height within the canopy. Assuming the dispersive

shear stress (4) is much smaller than the Reynolds stress, the decrease in $\langle \overline{u'w'} \rangle$ is necessary to balance the aerodynamic drag of the foliage.

(ii) Well above the canopy ($z > 2h$) the ratios of second moments take standard, ISL values of $\sigma_u/u_* \simeq 2.5$; $\sigma_w/u_* \simeq 1.25$ (Garratt 1992), implying $r_{uw} = \overline{u'w'}/(\sigma_u \sigma_w)$ is about $-0.32$, while just above the canopy $\sigma_u/u_* \simeq 2.0$; $\sigma_w/u_* \simeq 1.1$, so that $r_{uw}$ decreases to about $-0.5$.

(iii) Within the RSL the gradient of mean wind speed or scalar concentration is weaker than would be the case if the MOST formulae applied all the way down to the canopy top (e.g. Chen & Schwerdtfeger 1989). Hence in the RSL, a given turbulent flux is supported by a weaker mean gradient than in the ISL above, and MOST 'phi functions' must be modified (Raupach 1979, 1992).

(iv) Streamwise and vertical skewnesses ($Sk_u$, $Sk_w$) are small well above the canopy ($z > 2h$) but large within where $1.0 \geqslant Sk_u \geqslant 0.5$ and $-0.5 \geqslant Sk_w \geqslant -1.0$. Associated with these large skewnesses are significant values of the turbulent-transport terms in second-moment budgets, so that the turbulence in the canopy/RSL is not in local equilibrium (Katul *et al.* 2006).

(v) Single- and multi-point measurements in wind tunnels show horizontal and vertical Eulerian integral length scales of order $h$ and convection velocities of the dominant turbulent motions approximately equal to $2\langle \overline{u} \rangle(h)$ through the canopy (Shaw *et al.* 1995; Finnigan 2000). This is in contrast to the ISL in which these quantities scale on distance from the ground or displacement plane.

(vi) The rates of convergence of EOF (also called principal orthogonal decomposition or principal component analysis) spectra are a sensitive test of the presence of coherent structures in turbulent flows. EOF analysis of wind-tunnel-model canopy data by Finnigan & Shaw (2000) and of the present LES data shows that the spectral convergence rate in the canopy/RSL is significantly more rapid than in the ISL.

(vii) The quadrant-hole technique has been widely applied to both smooth- and rough-wall turbulent boundary layers. Grass (1971) was the first to point out that close to rough surfaces, the sweep quadrant Q4 ($u' > 0$, $w' < 0$) dominates momentum transport, whereas throughout the rest of the boundary layer, the ejection quadrant Q2 ($u' < 0$, $w' > 0$) is much larger. This is in marked contrast to smooth-wall boundary layers in which the ejection quadrant Q2 is dominant almost all the way to the wall. In the canopy/RSL Q4 sweeps dominate momentum and scalar transfer, the ratio Q2/Q4 becoming larger than 1.0 around $z = 2h$ or lower and rising to 1.5 within the ISL (Finnigan 1979, 2000; Shaw, Tavanger & Ward 1983; Katul *et al.* 2007).

(viii) Further details of the relationship of sweeps and ejections to large-scale coherent structures spanning the canopy/RSL have been revealed by more elaborate conditional-sampling techniques such as compositing (Gao *et al.* 1989; Shaw & Paw U 1989; Gardiner, 1994) and wavelet transforms (Collineau & Brunet 1993*a*, *b*; Katul & Vidakovic 1998). In particular, sweeps are large infrequent coherent events transferring large quanta of stress; ejections are smaller and more frequent – they cut off at around half the hole size that sweeps do. Quadrant-hole analysis and allied conditional-sampling techniques are reviewed in the canopy context in Finnigan & Shaw (2000).

## Appendix B. Coincidence of pressure peaks and sweeps/ejections

Tests were performed to determine the relationship between sweeps and ejections during events detected by regions of overpressure of given magnitude at the canopy

top, $z = h$. Pressure peaks were detected by selecting minimum and maximum values for pressure but excluding peaks that were exceeded in value by another point at $z = h$ within plus or minus a horizontal distance $r = \sqrt{x^2 + y^2} = h$. The mean pressure of all realizations was subtracted off all values of pressure, and no normalization was performed. The standard deviation of pressure based on all realizations was 1.457.

For each detected pressure peak, upstream and downstream regions were examined for the presence of, respectively, a sweep and an ejection. This test was performed at $z = h$. The zones examined spanned a distance equal to $\pm h$ in the $x$ direction and $\pm 0.7h$ in the $y$ direction centred either immediately upstream or immediately downstream of the peak-pressure location. If the value of $u'w'$ met the criterion at any one point within the zone, it was declared a 'hit'. Sweeps were defined as $u' > 0$, $w' < 0$ and $u'w'$ more negative than a specified value for the sweep. Ejections were defined as $u' < 0$, $w' > 0$ and $u'w'$ more negative than a specified value for the ejection. Velocities were not normalized. Threshold values of $u'w'$ for sweeps and ejections were based on the average values of $\overline{u'w'}$ for Q4 events (mean $\overline{u'w'} = -1.047$) and for Q2 events (mean $\overline{u'w'} = -0.631$) based on all realizations.

| Pressure minimum ($m^2\,s^{-2}$) | Press maximum ($m^2\,s^{-2}$) | Sweep threshold ($m^2\,s^{-2}$) | Ejection threshold ($m^2\,s^{-2}$) | Pressure hits | Pressure + sweep | Pressure + ejection | Pressure + sweep + ejection | Ejection given sweep | Sweep given ejection |
|---|---|---|---|---|---|---|---|---|---|
| 1 | 2 | −0.5 | −0.3 | 684 | 493<br>72 % | 547<br>80 % | 361<br>53 % | 73 % | 66 % |
| 1 | 2 | −1.0 | −0.6 | 684 | 385<br>56 % | 478<br>70 % | 217<br>32 % | 56 % | 45 % |
| 2 | 3 | −0.5 | −0.3 | 671 | 594<br>89 % | 541<br>81 % | 472<br>70 % | 79 % | 87 % |
| 2 | 3 | −1.0 | −0.6 | 671 | 520<br>77 % | 470<br>70 % | 349<br>52 % | 67 % | 74 % |
| 3 | 4 | −0.5 | −0.3 | 395 | 387<br>98 % | 327<br>83 % | 319<br>81 % | 82 % | 98 % |
| 3 | 4 | −1.0 | −0.6 | 395 | 367<br>93 % | 273<br>69 % | 249<br>63 % | 68 % | 91 % |

Given the detection of a pressure pulse, there is a high likelihood of the presence of an upstream sweep and of a downstream ejection. The numbers are high (up to 98 % for a sweep and up to 83 % for an ejection) when large pressure thresholds are examined and thresholds for $u'w'$ are relatively low (half their mean values). The numbers are lowest when a low value is selected for the pressure threshold but relatively large $u'w'$ thresholds are chosen.

Given an upstream sweep or a downstream ejection, there is a high likelihood of the accompanying element on the other side of the pressure peak. It does not appear that sweeps commonly occur without ejections, or vice versa.

## REFERENCES

Adrian, R. J. 2007 Hairpin vortex organization in wall turbulence. *Phys. Fluids* **19**, 041301-1–041301-16.

Adrian, R. J., Meinhart, C. D. & Tomkins, C. D. 2000 Vortex organization in the outer region of the turbulent boundary layer. *J. Fluid Mech.* **422**, 1–54.

Baldocchi, D. D., Falge, E., Gu, L., Olson, R., Hollinger, D., Running, S., Anthoni, P., Bernhofer, C., Davis, K., Evans, R., Fuentes, J., Goldstein, A., Katul, G., Law, B., Lee, X., Malhi, Y., Meyers, T., Munger, W., Oechal, W., Paw U, K. T., Pilegaard, K., Schmid, H. P., Valentini, R., Verma, S., Vesala, T., Wilson, K. & Wofsy, S. 2001 FLUXNET: a new

tool to study the temporal and spatial variability of ecosystem-scale carbon dioxide, water vapour and energy flux densities. *Bull. Am. Meteorol. Soc.* **82**, 2415–2434.

Baldocchi, D. D. & Hutchinson, B. A. 1987 Turbulence in an almond orchard: vertical variation in turbulence statistics. *Boundary-Layer Meteorol.* **40**, 177–146.

Bohm, M., Finnigan, J. J. & Raupach, M. R. 2000 Dispersive fluxes and canopy flows: just how important are they? In *Proceedings of 24th Conference on Agricultural and Forest Meteorology*, American Meteorological Society, Davis, CA.

Brown, G. L. & Roshko, A. 1974 On density effects and large structure in turbulent mixing layers. *J. Fluid Mech.* **64**, 775–816.

Brown, K. W. & Covey, W. 1966 The energy-budget evaluation of the micro-meteorological transfer process within a corn field. *Agric. Meteorol.* **3**, 73–96.

Brunet, Y., Finnigan, J. J. & Raupach, M. R. 1994 A wind tunnel study of air flow in waving wheat: single-point velocity statistics. *Boundary-Layer Meteorol.* **70**, 95–132.

Butler, K. M. & Farrell, B. F. 1992 Three-dimensional optimal perturbations in viscous shear flow. *Phys. Fluids* A **8**, 1637–1650.

Cellier, P. & Brunet, Y. 1992 Flux-gradient relationships above tall plant canopies. *Agric. Forest Meteorol.* **58**, 93–117.

Chakraborty, P., Balachandar, S. & Adrian, R. J. 2005 On the relationships between local vortex identification schemes. *J. Fluid Mech.* **535**, 189–214.

Chen, F. & Schwerdtfeger, P. 1989 Flux-gradient relationships above tall plant canopies. *Quart. J. R. Meteorol. Soc.* **115**, 335–352.

Christen, A. & Vogt, R. 2004 Direct measurement of dispersive fluxes within a cork oak plantation. In *Proceedings of 26th Conference on Agricultural and Forest Meteorology*, American Meteorological Society, Vancouver, BC, Canada.

Christensen, K. T. & Adrian, R. J. 2001 Statistical evidence of hairpin vortex packets in wall turbulence. *J. Fluid Mech.* **431**, 433–443.

Coceal, O., Dobre A., Thomas, T. G. & Belcher, S. E. 2007 Structure of turbulent flow over regular arrays of cubical roughness. *J. Fluid Mech.* **589**, 375–409.

Collineau, S. & Brunet, Y. 1993*a* Detection of turbulent coherent motions in a forest canopy. Part 1. Wavelet analysis. *Boundary-Layer Meteorol.* **65**, 357–379.

Collineau, S. & Brunet, Y. 1993*b* Detection of turbulent coherent motions in a forest canopy. Part 2. Timescales and conditional averages. *Boundary-Layer Meteorol.* **66**, 49–73.

Deardorff, J. W. 1980 Stratocumulus-capped mixed layers derived from a three-dimensional model. *Boundary-Layer Meteorol.* **18**, 495–527.

Drazin, P. G. & Reid, W. H. 1981 *Hydrodynamic Stability*. Cambridge University Press.

Dwyer, M. J., Patton, E. G. & Shaw, R. H. 1997 Turbulent kinetic energy budgets from a large-eddy simulation of airflow above and within a forest. *Boundary-Layer Meteorol.* **84**, 23–43.

Finnigan, J. J. 1979 Turbulence in waving wheat. Part 2. Structure of momentum transfer. *Boundary-Layer Meteorol.* **16**, 213—236.

Finnigan, J. J. 1985 Turbulent transport in flexible plant canopies. In *The Forest–Atmosphere Interaction* (ed. B. A. Hutchison & B. B. Hicks), pp. 443–480. Reidel.

Finnigan, J. J. 2000 Turbulence in plant canopies. *Annu. Rev. Fluid Mech.* **32**, 519–571.

Finnigan, J. J. & Shaw, R. H. 2000 A wind tunnel study of airflow in waving wheat: an empirical orthogonal function analysis of the large-eddy motion. *Boundary-Layer Meteorol.* **96**, 211–255.

Finnigan, J. J. & Shaw, R. H. 2008 Double-averaging methodology and its application to turbulent flow in and above vegetation canopies. *Acta Geophys.* **5**, 534–561.

Fitzmaurice, L., Shaw, R. H., Paw U, K. T. & Patton, E. G. 2004 Three-dimensional scalar microfront systems in a large-eddy simulation of vegetation canopy flow. *Boundary-Layer Meteorol.* **112**, 107–127.

Frederiksen, J. S. & Branstator, G. 2005 seasonal variability of teleconnection patterns. *J. Atmos. Sci.* **62**, 1346–1365.

Gao, W., Shaw, R. H. & Paw U, K. T. 1989 Observation of organized structure in turbulent flow within and above a forest canopy. *Boundary-Layer Meteorol.* **47**, 349–377.

Gardiner, B. A. 1994 Wind and wind forces in a plantation spruce forest. *Boundary-Layer Meteorol.* **67**, 161–186.

Garratt J. R. 1980 Surface influence on vertical profiles in the atmospheric near-surface layer. *Quart. J. R. Meteorol. Soc.* **106**, 803–819.

Garratt J. R. 1983 Surface influence upon vertical profiles in the nocturnal boundary layer. *Boundary-Layer Meteorol.* **26**, 69–80.

Gerz, T., Howell, J. & Mahrt, L. 1994 Vortex structures and microfronts. *Phys. Fluids* **6**, 1242–1251.

Ghisalberti, M. & Nepf, H. 2002 Mixing layers and coherent structures in vegetated aquatic flow. *J. Geophys. Res.* **107**, 1–11.

Grass, A. J. 1971 Structural features of turbulent flow over smooth and rough boundaries. *J. Fluid Mech.* **50**, 233–255.

Haidari, A. H. & Smith C. R. 1994 The generation and regeneration of single hairpin vortices. *J. Fluid Mech.* **277**, 135–162.

Harman, I. N. & Finnigan, J. F. 2007 A simple unified theory for flow in the canopy and roughness sublayer. *Boundary-Layer Meteorol.* **123**, 339–363.

Harman, I. N. & Finnigan, J. F. 2008 Scalar concentration profiles in the canopy and roughness sublayer. *Boundary-Layer Meteorol.* **129**, 323–351.

Head, M. & Bandyopadhyay, P. 1981 New aspects of turbulent boundary layer structure. *J. Fluid Mech.* **107**, 297–338.

Holmes, P., Lumley, J. L. & Berkooz, G. 1996 *Turbulence, Coherent Structures, Dynamical Systems and Symmetry*. Cambridge University Press.

Hunt, J. C. R. & Carruthers, D. J. 1990 rapid distortion theory and the 'problems' of turbulence. *J. Fluid Mech.* **212**, 497–532.

Hunt, J. C. R. & Morrison, J. F. 2000 Eddy structure in turbulent boundary layers. *Eur. J. Mech.* .B **19**, 673–694.

Jeong, J. & Hussain, F. 1995 On the identification of a vortex. *J. Fluid Mech.* **285**, 69–94.

Jeong, J., Hussain, F., Schoppa, W. & Kim, J. 1997 Coherent structures near the wall in a turbulent channel flow. *J. Fluid Mech.* **332**, 185–214.

Kaimal, J. C. & Finnigan, J. J. 1994 *Atmospheric Boundary Layer Flows: Their Structure and Measurement*. Oxford University Press.

Katul, G. & Vidakovic, B. 1998 Identification of low-dimensional energy containing/flux transporting eddy motion in the atmospheric surface layer using wavelet thresholding methods. *J. Atmos. Sci.* **55**, 377–389.

Katul, G. G., Poggi, D., Cava, D. & Finnigan, J. J. 2006 The relative importance of ejections and sweeps to momentum transfer in the atmospheric boundary layer. *Boundary-Layer Meteorol.* **120**, 367–375.

Kim, J. & Moin, P. 1986 The structure of the vorticity field in turbulent channel flow. Part 2. Study of ensemble-averaged fields. *J. Fluid Mech.* **162**, 339–363.

Leonard, A. 1974 Energy cascade in large-eddy simulations of turbulent fluid flows. *Adv. Geophys.* **18A**, 237–248.

Liu, J. T. C. 1988 Contributions to the understanding of large-scale coherent structures in developing free turbulent shear flows. *Adv. Appl. Mech.* **26**, 183–309.

Liu, Z., Adrian, R. J. & Hanratty, T. J. 2001 Large-scale modes of turbulent channel flow: transport and structure. *J. Fluid Mech.* **448**, 53–80.

Lu, S. S. & Willmarth, W. W. 1973 Measurements of the structure of Reynolds stress in a turbulent boundary layer. *J. Fluid Mech.* **60**, 481–571.

Lumley, J. L. 1967 The structure of inhomogeneous turbulent flows. In *Atmospheric Turbulence and Radio Wave Propagation* (ed. A. M. Yaglom & V. I. Tatarsky), p. 166. Nauka.

McKeon, B. J. & Sreenivasen, K. R. 2007 Introduction: scaling and structure in high Reynolds number wall-bounded flows. *Phil. Trans. R. Soc.* A **365**, 635–646.

Michalke, A. 1964 On the inviscid instability of the hyperbolic-tangent velocity profile. *J. Fluid Mech.* **19**, 543–556.

Michalke, A. 1965 On spatially growing disturbances in an inviscid shear layer. *J. Fluid Mech.* **23**, 521–544.

Moin, P. & Kim, J. 1985 The structure of the vorticity field in a turbulent channel flow. part 1. analysis of the instantaneous fields and statistical correlations. *J. Fluid Mech.* **155**, 441–464.

Moin, P. & Moser, R. D. 1989 Characteristic-eddy decomposition of turbulence in a channel. *J. Fluid Mech.* **200**, 471–509.

Mölder, M., Grelle, A., Lindroth, A. & Halldin, S. 1999 Flux-profile relationships over a boreal forest-roughness sublayer corrections. *Agric. Forest Meteorol.* **98–99**, 645–658.

Moser, R. D. & Rogers M. M. 1993 The three-dimensional evolution of a plane mixing layer: pairing and the transition to turbulence. *J. Fluid Mech.* **247**, 275–320.

Patton, E. G., Davis, K. J., Barth, M. C. & Sullivan, P. P. 2001 Decaying scalars emitted by a forest canopy – a numerical study. *Boundary-Layer Meteorol.* **100**, 91–129.

Patton, E. G., Sullivan, P. P. & Davis, K. J. 2003 The influence of a forest canopy on top-down and bottom-up diffusion in the planetary boundary layer. *Quart. J. R. Meteorol. Soc.* **129**, 1415–1434.

Patton, E. G., Sullivan, P. P. & Moeng, C.-H. 2005 The influence of idealized heterogeneity on wet and dry planetary boundary layers coupled to the land surface. *J. Atmos. Sci.* **62**, 2078–2097.

Perry, A. E. & Maruic, I. 1995 A wall-wake model for the turbulence structure of boundary layers. Part 1. Extension of the attached eddy hypothesis. *J. Fluid Mech.* **298**, 361–388.

Pierrehumbert, R. T. & Widnall, S. E. 1982 The two- and three-dimensional instabilities of a spatially periodic shear layer. *J. Fluid Mech.* **112**, 467—474.

Raupach, M. R. 1979 Anomalies in flux-gradient relationships over forest. *Boundary-Layer Meteorol.* **16**, 467–486.

Raupach, M. R. 1992 Drag and drag partition on rough surfaces. *Boundary-Layer Meteorol.* **60**, 375–395.

Raupach, M. R., Coppin, P. A. & Legg, B. J. 1986 Experiments on scalar dispersion within a model plant canopy. Part 1. The turbulence structure. *Boundary-Layer Meteorol.* **35**, 21–52.

Raupach, M. R., Finnigan, J. J. & Brunet, Y. 1996 Coherent eddies and turbulence in vegetation canopies: the mixing layer analogy. *Boundary-Layer Meteorol.* **78**, 351–382.

Raupach, M. R. & Shaw, R. H. 1982 Averaging procedures for flow within vegetation canopies. *Boundary-Layer Meteorol.* **22**, 79–90.

Reynolds R. T., Hayden, P., Castro, I. P. & Robins, A. G. 2007 Spanwise variations in nominally two-dimensional rough-wall boundary layers. *Exp. Fluids* **42**, 311–320.

Robinson, S. K. 1991 Coherent motions in the turbulent boundary layer. *Annu. Rev. Fluid Mech.* **23**, 601–639.

Rogers, M. M. & Moin, P. 1987 The structure of the vorticity field in homogeneous turbulent flows. *J. Fluid Mech.* **176**, 33–66.

Rogers, M. M. & Moser, R. D. 1994 Direct simulation of a self-similar turbulent mixing layer. *Phys. Fluids* **6**, 903–923.

Shaw, R. H., Brunet, Y., Finnigan, J. J. & Raupach, M. R. 1995 A wind tunnel study of air flow in waving wheat: two-point velocity statistics. *Boundary-Layer Meteorol.* **76**, 349–376.

Shaw, R. H. & Patton, E. G. 2003 Canopy element influences on resolved- and subgrid-scale energy within a large-eddy simulation. *Agric. Forest Meteorol.* **115**, 5–17.

Shaw, R. H, Paw U. K. T., Zhang, X. J., Gao, W., Den hartog, G. & Neumann, H. H. 1990 Retrieval of turbulent pressure fluctuations at the ground surface beneath a forest. *Boundary-Layer Meteorol.* **50**, 319–338.

Shaw, R. H. & Schumann, U. 1992 Large-eddy simulation of turbulent flow above and within a forest. *Boundary-Layer Meteorol.* **61**, 47–64.

Shaw, R. H., Tavanger, J. & Ward, D. P. 1983 Structure of the Reynolds stress in a canopy layer. *J. Climate Appl. Meteorol.* **22**, 1922–1931.

Stuart, J. T. 1967 On finite amplitude oscillations in laminar mixing layers. *J. Fluid Mech.* **29**, 417–440.

Sullivan, P. P., Horst, T. W., Lenschow, D. H., Moeng, Chin-Hoh & Weil, J. C. 2003 Structure of subfilter-scale fluxes in the atmospheric surface layer with application to large-eddy simulation modelling. *J. Fluid Mech.* **482**, 101–139.

Sullivan, P. P. & Patton, E. G. 2008 A highly parallel algorithm for turbulence simulations in planetary boundary layers: results with meshes up to $1024^3$. Paper No. 11B5. In *Proceedings of 18th American Meteorological Society Symposium on Boundary Layers and Turbulence*. 9–13 June 2008, Stockholm, Sweden.

Theordorsen, T. 1952 Mechanism of turbulence. In *Proceedings of Second Midwestern Conference on Fluid Mechanics*. Ohio State University, Columbus, OH.

Thom, A. S. Stewart, J. B., Oliver, H. R. & Gash, J. H. C. 1975 Comparison of aerodynamic and energy budget analysis of fluxes over a pine forest. *Quart. J. R. Meteorol. Soc.* **101**, 93–105.

Tomkins, C. D. & Adrian, R. J. 2003 Spanwise structure and scale growth in turbulent boundary layers. *J. Fluid. Mech.* **490**, 37–74.

Townsend, A. A. 1976 *The Structure of Turbulent Shear Flow*. Cambridge University Press.

Watanabe, W. 2004 Large-eddy simulation of coherent turbulence structures associated with scalar ramps over plant canopies. *Boundary-Layer Meteorol.* **112**, 307–341.

White, B. L. & Nepf, H. M. 2007 Shear instability and coherent structures in shallow flow adjacent to a porous layer. *J. Fluid Mech.* **593**, 1–32.

Widnall, S. E. 1975 The structure and dynamics of vortex filaments. *Annu. Rev. Fluid Mech.* **7**, 141–165.

Winant, C. & Browand, F. 1974 Vortex pairing, the mechanism of turbulent mixing layer growth at moderate Reynolds number. *J. Fluid Mech.* **63**, 237–255.

Wyngaard, J. C. 1982 Boundary layer modelling. In *Atmospheric Turbulence and Air Pollution Meteorology* (ed. F. T. M. Nieuwstadt & H. van Dop), pp. 69–106, Reidel.

Zhang, S. & Choudhury, D. 2006 Eigen helicity density: a new vortex identification scheme and its application in accelerated inhomogeneous flows. *Phys. Fluids* **18** 058104-1–058104-4.

Zhou, J., Adrian, R. J., Balachandar, S. & Kendall, T. M. 1999 Mechanisms for generating coherent packets of hairpin vortices in channel flow. *J. Fluid Mech.* **387**, 353–396.